

RESEARCH ARTICLE | OCTOBER 20 2023

Atomically smooth films of CsSb: A chemically robust visible light photocathode ^F

C. T. Parzyck ¹; C. A. Pennington ¹; W. J. I. DeBenedetti ¹; J. Balajka ¹; E. M. Echeverria ¹; H. Paik ¹; L. Moreschini ¹; B. D. Faeth ¹; C. Hu ¹; J. K. Nangoi ¹; V. Anil ¹; T. A. Arias; M. A. Hines ¹; D. G. Schlom ¹; A. Galdi ¹; K. M. Shen ¹; J. M. Maxson



APL Mater. 11, 101125 (2023)
<https://doi.org/10.1063/5.0166334>



CrossMark

yttrium iron garnet, zeolites, nano ribbons, sapphire windows, spintronics, silver nanoparticles, MOCVD, rare earth metals, osmium, refractory metals, anodic aluminum oxide, niobate, InAs wafers, perovskite crystals, transparent ceramics, MOFs, AuNPs, ZnS, CdTe

Li	Be	B	C	N	O	F	Ne										
Na	Mg	Al	Si	P	S	Cl	Ar										
K	Ca	Sc	Ti	V	Cr	Mn	Fe	Co	Ni	Cu	Zn	Ga	Ge	As	Se	Br	Kr
Rb	Sr	Y	Zr	Nb	Mo	Tc	Ru	Rh	Pd	Ag	Cd	In	Sn	Sb	Te	I	Xe
Cs	Ba	La	Hf	Ta	W	Re	Os	Ir	Pt	Au	Hg	Tl	Pb	Bi	Po	At	Rn
Fr	Ra	Ac	Rf	Db	Sg	Bh	Hs	Mt	Ds	Rg	Cn	Nh	Fl	Mc	Lv	Ts	Og
Ce	Pr	Nd	Pm	Sm	Eu	Gd	Tb	Dy	Ho	Er	Tm	Yb	Lu				
Th	Pa	U	Np	Pu	Am	Cm	Bk	Cf	Es	Fm	Md	No	Lr				

cerium oxide polishing powder, surface functionalized nanoparticles, cermet, nanodispersions, MBE grade materials, thin film, OLED lighting, solar energy, sputtering targets, fiber optics, h-BN, deposition slugs, CVD precursors, photovoltaics, metamaterials, borosilicate glass, YBCO superconductors, InGaAs, indium tin oxide, MgF2, rutile, diamond micropowder, optical glass

additive manufacturing, organometallics, transparent ceramics, CIGS, transparent ceramics, CIGS, cermet, nanodispersions, MBE grade materials, thin film, OLED lighting, solar energy, sputtering targets, fiber optics, h-BN, deposition slugs, CVD precursors, photovoltaics, metamaterials, borosilicate glass, YBCO superconductors, InGaAs, indium tin oxide, MgF2, rutile, diamond micropowder, optical glass

The Next Generation of Material Science Catalogs

www.americanelements.com
© 2001-2022, American Elements LLC, a U.S. Registered Trademark

Atomically smooth films of CsSb: A chemically robust visible light photocathode

Cite as: APL Mater. 11, 101125 (2023); doi: 10.1063/5.0166334

Submitted: 4 July 2023 • Accepted: 25 September 2023 •

Published Online: 20 October 2023


















View Online



Export Citation



CrossMark

C. T. Parzyck,¹  C. A. Pennington,²  W. J. I. DeBenedetti,^{3,a)}  J. Balajka,³  E. M. Echeverria,² 
H. Paik,^{4,5,6}  L. Moreschini,⁴  B. D. Faeth,⁴  C. Hu,¹  J. K. Nangoi,¹  V. Anil,¹  T. A. Arias,¹
M. A. Hines,³  D. C. Schlom,^{7,8,9}  A. Galdi,^{2,10,b)}  K. M. Shen,^{1,8}  and J. M. Maxson^{2,b)}

AFFILIATIONS

¹Laboratory of Atomic and Solid State Physics, Department of Physics, Cornell University, Ithaca, New York 14853, USA

²Cornell Laboratory for Accelerator-Based Sciences and Education, Cornell University, Ithaca, New York 14853, USA

³Department of Chemistry and Chemical Biology, Cornell University, Ithaca, New York 14853, USA

⁴Platform for the Accelerated Realization, Analysis, and Discovery of Interface Materials (PARADIM), Cornell University, Ithaca, New York 14853, USA

⁵School of Electrical and Computer Engineering, University of Oklahoma, Norman, Oklahoma 73019, USA

⁶Center for Quantum Research and Technology, University of Oklahoma, Norman, Oklahoma 73019, USA

⁷Department of Materials Science and Engineering, Cornell University, Ithaca, New York 14853, USA

⁸Kavli Institute at Cornell for Nanoscale Science, Cornell University, Ithaca, New York 14853, USA

⁹Leibniz-Institut für Kristallzüchtung, Max-Born-Straße 2, 12489 Berlin, Germany

¹⁰Department of Industrial Engineering, University of Salerno, Fisciano (SA) 84084, Italy

^{a)} Authors to whom correspondence should be addressed: agaldi@unisa.it and jmm586@cornell.edu

^{b)} Present address: Los Alamos National Laboratory, Los Alamos, New Mexico 87544, United States.

ABSTRACT

Alkali antimonide semiconductor photocathodes provide a promising platform for the generation of high-brightness electron beams, which are necessary for the development of cutting-edge probes, including x-ray free electron lasers and ultrafast electron diffraction. Nonetheless, to harness the intrinsic brightness limits in these compounds, extrinsic degrading factors, including surface roughness and contamination, must be overcome. By exploring the growth of Cs_xSb thin films monitored by *in situ* electron diffraction, the conditions to reproducibly synthesize atomically smooth films of CsSb on 3C-SiC (100) and graphene-coated TiO₂ (110) substrates are identified, and detailed structural, morphological, and electronic characterization is presented. These films combine high quantum efficiency in the visible (up to 1.2% at 400 nm), an easily accessible photoemission threshold of 566 nm, low surface roughness (down to 600 pm on a 1 μm scale), and a robustness against oxidation up to 15 times greater than Cs₃Sb. These properties lead us to suggest that CsSb has the potential to operate as an alternative to Cs₃Sb in electron source applications where the demands of the vacuum environment might otherwise preclude the use of traditional alkali antimonides.

© 2023 Author(s). All article content, except where otherwise noted, is licensed under a Creative Commons Attribution (CC BY) license (<http://creativecommons.org/licenses/by/4.0/>). <https://doi.org/10.1063/5.0166334>

I. INTRODUCTION

High-brightness electron beams are an essential ingredient in a variety of modern scientific applications, which require high charge and ultrashort electron pulses. These applications range from x-ray free electron lasers (FELs)^{1,2} to fs-scale ultrafast electron microscopes^{3–5} and to electron-based hadron cooling systems

and electron linear colliders.^{6–8} Generation of pulsed electron beams is accomplished via photoemission of electrons from specifically tailored materials characterized by high quantum efficiency (QE, photoemitted electrons per incident photon). To ensure high brightness of the resulting beam, the intrinsic emittance of the material (a measurement of the momentum spread of the photoelectrons) must be minimized⁹ by limiting the physical and chemical

roughness of the surface of the sample.¹⁰ One class of materials identified by accelerator scientists as high efficiency photocathode candidates are alkali antimonide semiconductors: $AA'_2\text{Sb}$ ($A, A' = \text{Cs, K, Na, Rb}$, including $A = A'$).¹¹ These compounds are characterized by QE's of 10^{-2} to 10^{-1} at ~ 550 nm¹² and by mean transverse energies (MTEs) below 180 meV at 532 nm, which can be further reduced by operating near the photoemission threshold and at low temperature. These low MTEs are relevant, for example, for next generation high repetition rate FELs.^{11,13} Unfortunately, this class of materials is also extremely sensitive to oxidation—which tends to suppress the photocathode efficiency and enlarge the MTE.¹⁴ Alkali antimonides have stringent vacuum requirements, demanding pressures below 10^{-10} Torr to be handled without significant degradation,¹⁵ which limits the scope of their applicability. Additionally, the high vapor pressure of alkali metals at ambient temperatures presents a challenge to the synthesis of smooth, ordered films.^{16–19} Because surface disorder induces emittance degradation and reduces the utility of the photocathode, significant effort has been devoted to finding ways to reduce the crystalline disorder of these materials. Recent advances include both improving the as-grown film properties (smoothness, homogeneity) through new synthesis techniques^{20,21} as well as finding ways to increase their robustness against contamination and aging, for example by encapsulating them in 2D materials.^{22,23}

In this article, we explore the phase diagram of Cs_xSb using a variety of *in situ* and *operando* probes of the structure, morphology, and photoemission properties of the resulting films. We identify another member of the alkali antimonide family, CsSb , as a visible light photoemitter, which can be grown in crystalline, ultra-flat films characterized by surface roughness better than 1 nm on a $1\ \mu\text{m}$ scale and quantum efficiency up to 1.2% at 400 nm. This phase is found to be substantially more resilient to oxygen contamination than its more commonly synthesized cousin, Cs_3Sb , which may extend the operational lifetime of the cathodes in the demanding environment of a photoinjector cavity. The photoemission threshold of CsSb is found to be around 566 nm, close to the second harmonic of many high repetition rate lasers currently used in linear accelerator photoinjectors (~ 532 nm).²⁴ This means that near-threshold operation of CsSb photocathodes would be achievable without major modification to existing optical assemblies, in addition to making use of alkali antimonide deposition systems already in use in several accelerator laboratories.

The recent achievement of epitaxial single-oriented Cs_3Sb films¹⁹ was in large part made possible through the use of reflection high energy electron diffraction (RHEED) as a structural diagnostic during growth. This technique is a mainstay of traditional semiconductor, metal, and oxide film growth by molecular-beam epitaxy (MBE); however, to date, it has been infrequently employed in photocathode preparation, where the traditional *operando* diagnostic is the QE.^{25,26} By monitoring the structure of the sample during deposition, using RHEED, we identify various growth regimes of Cs_xSb as a function of the growth temperature, including the stabilization of ordered films of CsSb . We study the chemical composition of the resulting films using x-ray photoemission spectroscopy (XPS), their morphology using scanning tunneling microscopy (STM), and their electronic structure using angle resolved photoemission spectroscopy (ARPES).

II. SYNTHESIS

We begin with an overview of the growth of Cs_xSb photocathodes over a range of conditions with the structure monitored during growth using RHEED and the QE measured directly afterward. Because the cesium desorption rate from the sample is strongly temperature dependent on the range explored here, adsorption control of the stoichiometry can be accomplished by oversupplying cesium and varying the substrate temperature, rather than by varying the Cs:Sb flux ratio. The quantum efficiency of a set of samples grown under similar flux conditions (cf. Sec. VIII A) is depicted in Fig. 1(a). Using RHEED, we identify three distinct regimes of film growth across the explored temperature range. At low temperatures, regime (I), around 40°C , the high efficiency Cs_3Sb phase is formed with QE ranging from 3% to 10%. When films are codeposited at this temperature, they are polycrystalline and form textured ring patterns in RHEED, shown in Fig. 1(b). Once formed, however, this phase is stable against Cs loss at higher temperatures and can be annealed up to $\sim 85^\circ\text{C}$ to order the domains and, on an appropriate substrate, produce an epitaxial film while maintaining 1% level QE in the green.¹⁹ When films are deposited at higher temperatures, $\sim 90^\circ\text{C}$, regime (II), the RHEED patterns show less well-defined rings and some faint streaks. While the QE of these samples remains reasonably high ($\sim 10^{-3}$ at 504 nm), RHEED indicates decreased crystallinity and a lack of ordering. However, when the substrate temperature is further increased, exceeding 100°C , regime (III), a new phase emerges,

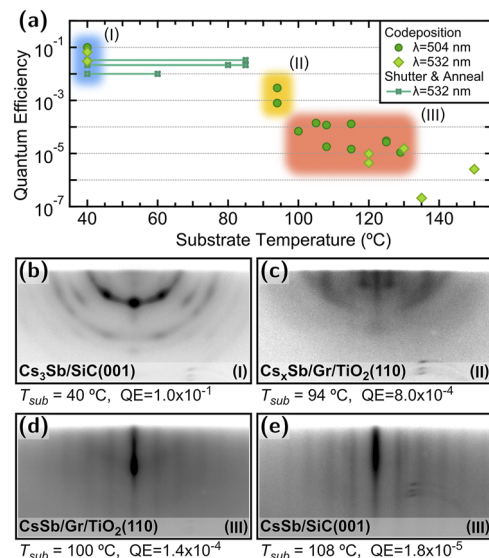


FIG. 1. Quantum efficiency (QE) of Cs_xSb photoemitters, $1 \leq x \leq 3$. (a) QE (in the green) as a function of growth temperature. Samples grown by codeposition at a single temperature are shown as circles and diamonds; samples using the solid-phase epitaxy approach of Ref. 19 are depicted as lines connecting the deposition and annealing temperatures. (b) RHEED pattern of a 18.6 nm thick, textured, high-efficiency Cs_3Sb film grown at low temperature. (c) RHEED pattern of a 14 nm thick, textured, medium-efficiency film in the intermediate regime. (d) and (e) RHEED patterns of 14 nm thick, fiber-texture CsSb films codeposited at temperatures above 100°C . (b)–(e) A logarithmic intensity scale is used; quoted QEs are measured at 504 nm.

which is characterized by the streaked RHEED pattern shown in Figs. 1(d) and 1(e). Spectroscopic measurements identify the stoichiometry of this phase to be CsSb. No azimuthal dependence of the RHEED streaks is observed, indicating no preferential in-plane orientation of the films. Nonetheless, the absence of rings indicates alignment of the out-of-plane axes of the grains, and the lack of vertical modulation indicates smooth, terraced growth of a so-called “fiber textured” film.²⁷

The sample thicknesses can be estimated from the measured Sb flux and the areal number densities of the identified phases. All regime (III) samples were 14 nm thick, while the regime (II) samples were 14 nm [QE(504 nm) = 0.8×10^{-3}] and 74 nm [QE(504 nm) = 3×10^{-3}] thick. For comparison, the QE of the epitaxial Cs₃Sb samples, which are less than 10 nm thick,¹⁹ is about 2% at 532 nm. Therefore, the QE values associated with the three regimes are distinct, despite the expected variations due to thickness. Although the QE of films grown in regime (III) is reduced (ranging from 1.1×10^{-5} to 1.4×10^{-4} at 504 nm) compared to Cs₃Sb, these films remain visible light photoemitters. The growth window for this particular phase is $\sim 30^\circ\text{C}$ wide, with the quantum efficiency dropping below 10^{-5} at higher growth temperatures. For this film series, the growth windows were identified using Cs fluxes of $\sim 1.6 - 3.0 \times 10^{13}$ at/cm²/s; in general, the temperature boundaries are expected to depend on the chosen elemental flux owing to competition between deposition and re-evaporation of the Cs vapor at elevated growth temperatures.

The remainder of this work is concerned with the study of films in regimes (II) and (III), including their morphology and photoemission properties. We note that in regime (III), fiber-textured films are produced on both of the substrates investigated here, 3C-SiC (100) and monolayer graphene deposited on rutile TiO₂ (110). No discernible differences in either the RHEED patterns or QE were observed between films grown on the two substrates, indicating that they both provide reasonable platforms for the synthesis of CsSb.

III. X-RAY PHOTOELECTRON SPECTROSCOPY

In Figs. 2(a) and 2(b), we report the Cs 3*d* and Sb 3*d* XPS spectra of three Cs_{*x*}Sb samples grown on graphene/TiO₂ (110) at different substrate temperatures (T_{sub}): one in growth regime (II) ($T_{sub} = 94^\circ\text{C}$) and two grown at higher temperature in regime (III). In Fig. 2(a), the Cs 3*d*_{5/2} peak position is close to the Cs⁺

TABLE I. Composition of 14 nm thick CsSb samples obtained by XPS as a function of growth temperature, T_{sub} , and photoelectron emission angle: normal emission = 0° , grazing emission = 70° . At grazing emission, the probe depth is reduced by a factor of ~ 3 , enhancing sensitivity to the sample surface.

T_{sub} ($^\circ\text{C}$)	0°	70°
94	Cs _{0.51} O _{0.12} Sb _{0.37}	Cs _{0.53} O _{0.21} Sb _{0.26}
100	Cs _{0.48} O _{0.11} Sb _{0.41}	Cs _{0.51} O _{0.13} Sb _{0.36}
129	Cs _{0.48} O _{0.07} Sb _{0.45}	Cs _{0.49} O _{0.09} Sb _{0.41}

reference energy (752.2 eV) for all the samples, though some shift toward higher binding energies was observed with decreasing T_{sub} . The peak at ~ 730.9 eV is attributable to the Mg K α_3 satellite of the Cs 3*d*_{3/2} peak, although the intensity ratio between the peaks, exceeding 8%, does not exclude some plasmon contribution. In contrast to measurements of high QE Cs₃Sb²⁸ and metallic Cs,²⁹ no strong plasmon peaks were observed in these samples. The Sb 3*d*_{5/2} peak position, 527.45–527.65 eV, falls between the binding energies of Sb⁰ metal (528.3 eV) and Sb³⁻ in Cs₃Sb (526.1 eV) reference samples (a comparison is reported in the supplementary material). In previous studies of Cs–Sb compounds, this binding energy value has been attributed to Sb⁰ (either bulk or “atomic”),^{30,31} while others attributed it to different phases of the Cs–Sb system, such as CsSb or Cs₅Sb₄.¹⁴ However, evaluation of the Sb Auger parameter in the present films is consistent with reduced Sb in Cs₃Sb rather than with Sb metal. Estimates of the sample composition, reported in Table I, are close to Cs:Sb = 1:1, which leads us to attribute the observed Sb 3*d*_{5/2} binding energy value to Sb¹⁻ species.

To enhance surface sensitivity and examine the presence of surface oxidation, the spectra of Fig. 2 were collected in glancing emission.¹⁵ The O 1*s* spectrum ([528, 534] eV) overlaps with the Sb 3*d* peaks; the spin-orbit splitting of the Sb 3*d*_{3/2}–3*d*_{5/2} peaks can be exploited to isolate the oxygen contribution using the methods of Ref. 15; the results are shown in Fig. 2(c). In all three samples, we observe some contribution from oxygen species, likely originating from exposure during the vacuum suitcase sample transfer between the MBE and STM-XPS systems.^{19,25} For comparison, the XPS spectra measured *in situ*, reported in Figs. S5(c) and S6(a) of the supplementary material, do show appreciable spectral weight at the O 1*s* binding energies. We observe O 1*s* binding energies of

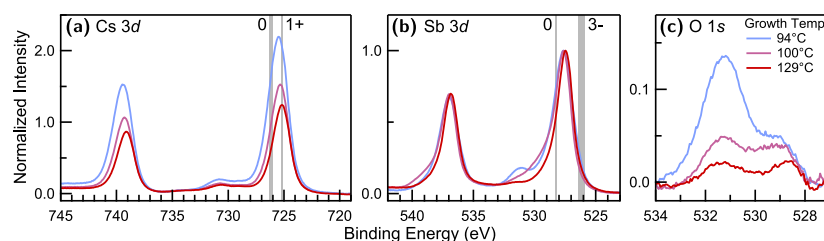


FIG. 2. Background subtracted XPS spectra in the (a) Cs 3*d*, (b) Sb 3*d*, and (c) O 1*s* regions for 14 nm thick samples grown at different substrate temperatures; intensity is normalized to the Sb 3*d*_{5/2} peak. Literature reference energies for Cs⁰, Cs¹⁺, and Sb³⁻ are provided as gray lines^{32–34} in addition to a metallic Sb sample (Sb⁰) measured in the same XPS system.¹⁹ Measurements presented here were performed at a grazing emission angle of 70° ; normal emission data are available in the supplementary material.

531.2 and 528.7–529 eV, the latter close to the expected Sb $3d_{3/2}$ satellite (~ 528.4 eV). Both energies fall into the range associated with metal oxides,²⁹ and in particular, the former is close to the binding energy associated with peroxide species in Cs_2O_2 (529.9–531.0 eV)³⁵ or with antimony suboxide.³⁶

The surface composition of the samples of Fig. 2 was obtained from the integrated intensity of Cs $3d$, Sb $3d$, and O $1s$ spectra normalized by their relative sensitivity factors and photoelectron escape depth; the results are reported in Table I. From the less surface-sensitive normal emission measurements, we observe that the Cs:Sb ratio is closest to 1:1 for the sample grown at higher temperature and that Cs content increases with decreasing growth temperature. All samples were stored and transferred simultaneously from the MBE to the STM-XPS system; thus, they received identical exposure to residual gasses. Therefore, the observed correlation between the lower oxygen content and reduced Cs:Sb ratio in samples grown at higher T_{sub} indicates that stoichiometric CsSb has an increased oxidation resistance over the Cs rich phases. The Cs and O content is higher in the more surface sensitive measurements at grazing emission, which is consistent with surface oxidation. However, the differences between the spectra at different emission angles (supplementary material) indicate that the compositional gradient through the samples is minor, when compared to the typical behavior of Cs_3Sb where Cs segregation is observed in response to any oxygen exposure.^{15,25} Using the methods described in Refs. 30 and 37, the XPS data can be modeled by a bottom layer with composition Cs:Sb $\approx 1:1$ covered by a surface layer with composition Cs:O $\approx 1:1$, consistent with a layer of Cs_2O_2 , although the model parameters cannot be unequivocally determined using only two emission angles. The observed shift of the Cs $3d$ binding energy, and the less pronounced one of the Sb $3d$ peak, can be explained by band-bending induced by Cs_2O_2 ,³⁸ analogous to observations of superficially oxidized Cs_3Sb .¹⁵ While a Cs_2O_2 layer is necessary to activate photoemission from GaAs at visible or infrared wavelengths, the absence of O $1s$ peaks in *in situ* XPS measurements performed immediately following the *in situ* QE measurements indicates that the oxide layer is not required for visible light photoemission in this material.

IV. SCANNING TUNNELING MICROSCOPY

The development of high-quality alkali antimonide thin films has been stymied by their propensity to form rough or disordered surfaces during growth, contributing to high MTEs of the photoemitted electrons.^{10,39} Recent advances, including the careful choice of substrate and growth temperature, have helped to mitigate the surface roughness of Cs_3Sb films,^{17,19,21} but the synthesis of atomically ordered films still requires a delicate multi-step shuttered growth procedure. One advantage of CsSb indicated by the RHEED patterns in Figs. 1(d) and 1(e) is that smooth, terraced films may be produced by codeposition at a single temperature. To quantify this, the morphology of a set of MBE-grown CsSb films [on monolayer graphene coated TiO_2 (110)] was investigated using STM, and the results are summarized in Fig. 3 and in the supplementary material. A sample grown in regime (II) at a lower temperature of $\sim 94^\circ\text{C}$ shows a rough and disordered grain structure with a characteristic grain size of ~ 85 nm (equivalent disk radius) and a root-mean-square (rms) roughness of 1.4 nm averaged over grains. The surface

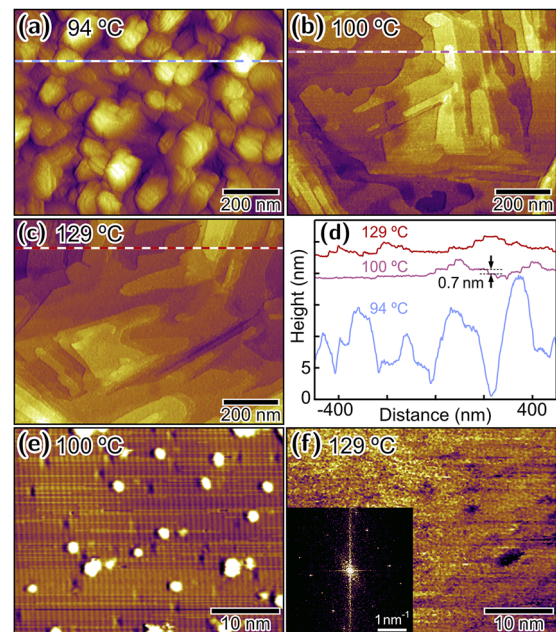


FIG. 3. STM images of 14 nm thick Cs_xSb films grown on graphene coated TiO_2 (110) substrates. (a)–(c) $1.0 \times 0.76 \mu\text{m}^2$ images of samples grown at 94, 100, and 129°C , respectively. (d) Line cuts from the marked areas in the prior three images; traces are offset for clarity. (e) and (f) Higher magnification images of terraces imaged in samples in (b) and (c), respectively; the inset shows the Fourier transform of the STM image.

roughness averaged over a $1 \times 1 \mu\text{m}^2$ area is found to be 2.3 nm. In contrast, samples grown at higher temperatures, in regime (III), show flat, smooth terraces, examples of which are shown in Figs. 3(b) and 3(c). The terrace-averaged rms roughness observed in Fig. 3(b) is only 240 pm (averaged over a lateral scale of ~ 200 nm) and is 600 pm when averaged on the $1 \mu\text{m}$ scale. The sample grown at higher temperature, in Fig. 3(c), shows a slightly increased rms roughness of 750 pm on the $1 \mu\text{m}$ scale. These roughness values compare favorably to state-of-the-art codeposited films of Cs_3Sb on SiC^{21} and SrTiO_3 .¹⁷

Figure 3(d) shows a set of representative line cuts from the previous three images. The blue line cut shows the morphology of a rough surface, while the pink and red lines show terrace widths and heights for the flat samples of Figs. 3(b) and 3(c). The terraces are separated by steps of roughly 0.7 nm, though there is some variation in the step heights measured across the STM maps, and step heights between 0.5 and 0.9 nm are observed. A higher magnification image of one of the terraces is given in Fig. 3(e), which shows atomic rows with both pits and islands, likely due to the presence of both atom vacancies and adatoms on the sample surface. The inter-row spacing is 0.79 nm, and the atomic rows change orientation at grain boundaries (cf. the supplementary material) as expected from the fiber-texture diffraction pattern observed in RHEED. Taken together, the RHEED and STM indicate that the films grow locally in ordered crystalline domains, with length scales of 100–200 nm, which are rotationally misaligned to form an even

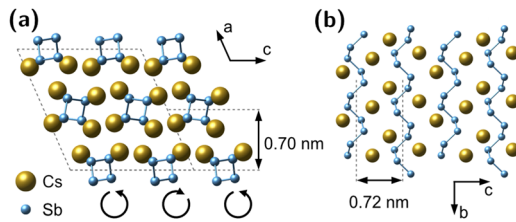


FIG. 4. Visualization of the crystal structure⁴² of the monoclinic phase, β -CsSb, measured in Ref. 41. (a) Projection along [010] showing the layered structure of the Sb spirals. Alternating layers have opposing tilts, and alternating columns have alternating chirality. (b) Structure of a single β -CsSb monolayer, viewed down the [100] axis, illustrating the quasi-1D structure of the Sb spirals.

distribution on the macroscale. As shown in Fig. 3(c), the terraced structure of the films is preserved throughout regime (III); from the Fourier transform of the STM image [Figs. 3(f) and 3(a)], a similar in-plane lattice constant of 0.76–0.78 nm can be extracted.

The aforementioned STM measurements of the film morphology are also consistent with prior studies of the bulk crystal structure of CsSb. It has been shown previously that bulk CsSb may crystallize in one of the two related structures; it was originally discovered that at higher temperatures (>500 °C) and longer reaction times (>100 h), a NaP-type orthorhombic phase with space group $P2_12_12_1$ forms.⁴⁰ Later, it was observed that at lower temperatures (~ 440 °C) and shorter reaction times (~ 1 h), a monoclinic phase may form with space group $P2_1/c$.⁴¹ Following Emmerling *et al.*,⁴¹ we term the high-temperature orthorhombic phase as α -CsSb and the lower temperature monoclinic phase as β -CsSb. Although the crystal symmetries differ, the α and β phases share a common structural motif, being composed of extended chains of Sb atoms surrounded in a cage of Cs ions—it is the relative orientation of the chains and their stacking sequence, which differentiates the two phases. A visualization of the β phase based on crystallography data reported in Ref. 41 is provided in Fig. 4, and the discussion of the α phase is provided in the supplementary material. For consistency, in both structures, we take the axis along the chains to be the [010] direction. In the β phase, the chirality of the Sb chains alternates across the (001) planes and the relative rotation of the chains alternates across (100). The β phase is composed of monolayers of chains stacked along the [100] direction with an expected spacing of 0.70 nm, which is also consistent with the measured STM step heights. Additionally, the row spacing expected from bulk measurements for (100) oriented β -CsSb is 0.72 nm, which is consistent with the above STM measurements. Note that presence of the α phase cannot be ruled out entirely by the measurements performed here as determination of the crystal symmetry by *ex situ* x-ray diffraction was not possible due to the air-sensitivity of the samples. Further refinement of the structure using *in situ* x-ray diffraction would help to clarify the precise phase stabilized under these growth conditions.

V. ANGLE-RESOLVED PHOTOEMISSION SPECTROSCOPY

Using *in situ* ARPES measurements and density functional theory (DFT) calculations, we can compare the measured electronic

structure of the MBE-grown CsSb films with the predicted band structure from prior bulk studies. A calculation of the band structure for bulk-like β -CsSb is shown in Fig. 5(a), and the corresponding calculation for the α phase is included in the supplementary material. Given the quasi-one-dimensional crystal structure, it is perhaps unsurprising that the resulting electronic structure is also quasi-one-dimensional. Paths parallel to the [010] axis (highlighted in blue) show dispersive features corresponding to hopping along the Sb–Sb chains. In contrast, paths perpendicular to [010], i.e., hopping across a more ionic Sb–Cs–Sb bond, show much flatter dispersion. Qualitatively, the band structures of the α and β phases are quite similar—the main difference arises from band splittings corresponding to the larger number of inequivalent Sb sites in the monoclinic cell. The DFT bandwidth of the near E_F manifold, primarily composed of Sb 5p states, is calculated to be 3.12 eV in the β phase and 3.06 eV in the α phase. These bandwidths are both substantially larger than those measured for the valence bands of Cs₃Sb, 1.2 eV,¹⁹ meaning that determination of the density of states by ARPES is a good metric for discriminating between the two phases [e.g., see the comparison in the supplementary material, Fig. S6(b)].

The density of states calculated by DFT matches well with *in situ* measurements of the valence band structure, in terms of both the peak structure and overall bandwidth, which is measured to be 3.55 eV in Fig. 5(b). The measured position of the Fermi level, at 620 meV above the valence band maximum, can be attributed to pinning of the chemical potential in the gap. This shift is similar to the DFT-calculated gap value of 520 meV—indicating that the Fermi level may lie at or near the conduction band minimum. While this suggests native electron doping, no weight is observed at E_F , so additional optical and electrical measurements are required to determine the true gap size and the carrier sign. We note that underestimation of the bandwidth (in this case by $\sim 14\%$) by the electronic structure calculation is similar to previous measurements of Cs₃Sb/SiC (100), where the observed bandwidth of the valence states is between 10% and 20% larger than the local-density approximation (LDA) prediction.¹⁹ In addition to the expected Sb 5p and Cs 6s states near the Fermi level, an additional peak is observed between 4.2 and 6.8 eV of binding energy—associated with the presence of oxygen 2p states. The calculated photoemission cross section for oxygen is enhanced over that of antimony in this energy range by a factor of 4.12,⁴⁵ so even superficial oxidation of the surface, as suggested by XPS measurements, may result in a large O 2p signal in ARPES. A more accurate representation of the oxygen DOS is included in the shaded region of Fig. 5(b) where the oxygen weight has been divided by its relative cross section. Finally, the weak peak observed at 7.5 eV is attributable to Sb 5s states, which have a diminished cross section (only 1.7% of σ_{Sb5p} at $h\nu = 21.2$ eV).⁴⁵

A consequence of the quasi-one-dimensional band structure is that when angle-resolved photoemission measurements are performed on these fiber-texture films, momentum resolved features are clearly visible, as shown in Figs. 5(c) and 5(d), taken with helium-I ($h\nu = 21.2$ eV) and krypton-I ($h\nu = 10.0$ eV) light, respectively. Using the fitted electron affinity, calculated bandgap, and measured work function, we estimate an inner potential⁴⁶ of $V_0 \sim 5.74$ eV, placing the out-of-plane momenta at 5.26 and 3.56 r.l.u. (1 r.l.u. = $2\pi/d_{(100)}$, $d_{(100)} = 13.92$ Å) for helium-I and krypton-I. At both photon energies, dispersive bands are visible

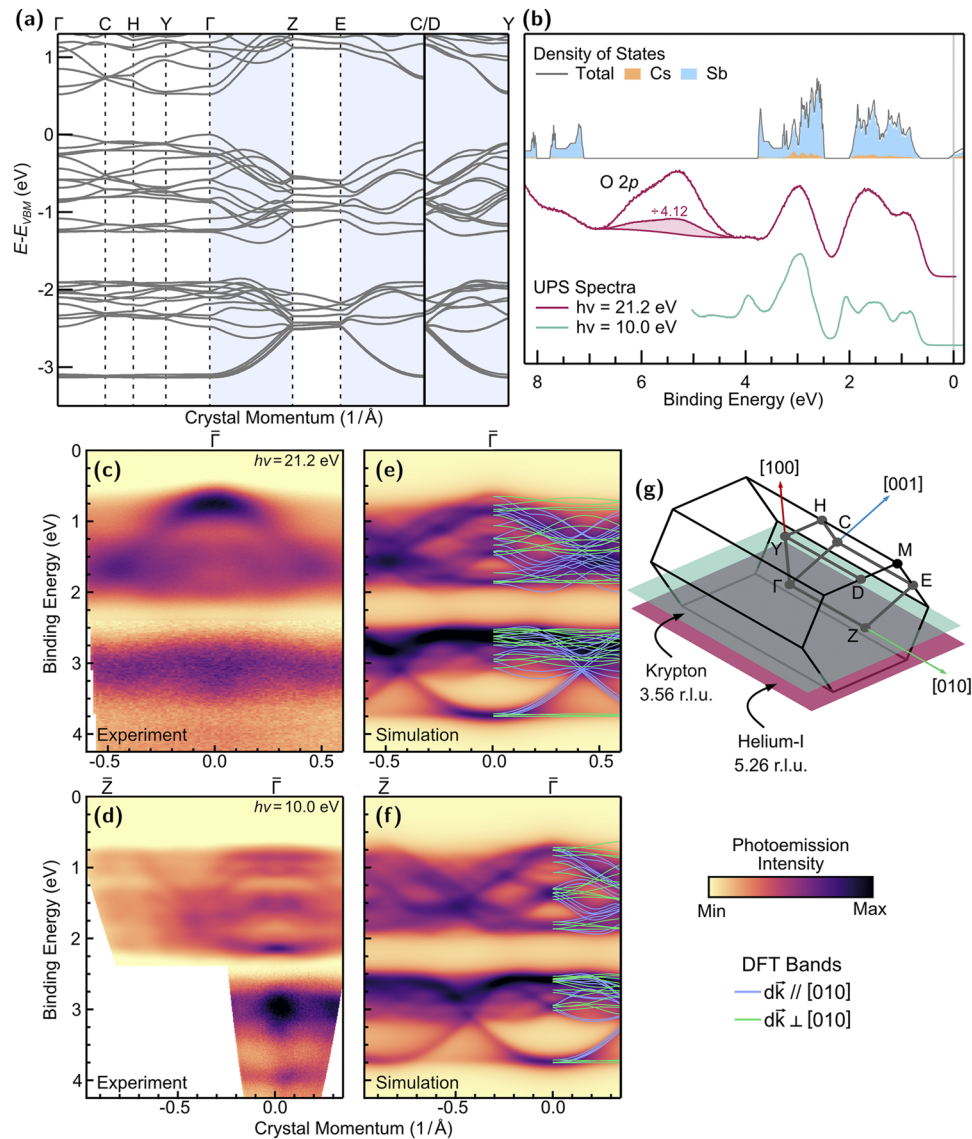


FIG. 5. Calculated and measured electronic structure of 14 nm thick CsSb films grown on SiC (100). (a) DFT calculation of the band structure of monoclinic β -CsSb. Cuts taken along directions parallel to the [010] axis are highlighted in blue. (b) Calculated density of states, with Cs and Sb contributions highlighted in orange and blue. Angle-integrated photoemission spectra illustrating the structure of the near E_F Sb 5p manifold in green and magenta. O 2p states are observed between 4.4 and 6.7 eV; their adjusted weight (divided by the ratio of the O/Sb photoemission cross sections ~ 4.12) is shaded. Composite angle-resolved spectra taken with helium-I ($h\nu = 21.2$ eV) and krypton-I ($h\nu = 10.0$ eV) light are shown in (c) and (d), respectively. Corresponding simulated spectra for a fiber-textured (100) oriented film are displayed in (e) and (f) at out-of-plane momenta of 5.26 and 3.56 r.l.u. (1 r.l.u. = $2\pi/d_{(100)}$ with $d_{(100)} \sim 13.92$ Å). Bands originating from specifically oriented domains are overlaid. (g) Brillouin zone^{43,44} of β -CsSb with the k -space path from (a) outlined in gray. Positions, in the folded zone scheme, of the ARPES cuts in (c) and (d) are highlighted in magenta and green, respectively.

between 0.75–2.25 and 2.50–4.00 eV, with a maximum observed at the center of the projected zone, consistent with the DFT calculation. The fact that the band structure is not completely washed away by the macroscopic rotational disorder is a consequence of the quasi-one dimensional nature of the structure: the measured spectrum is an incoherent sum over rotated domains with most of the

dispersion arising from domains where [010] is nearly aligned to the electron analyzer slit. Domains of other orientations contribute primarily flat bands and add up to a nearly momentum independent background.

More quantitatively, the spectra can be simulated by calculating a spectral function from the DFT band structure for each rotated

domain and then performing a sum over angles. The results of these calculations, at out-of-plane momenta corresponding to those of the ARPES measurements, are shown in Figs. 5(e) and 5(f). This simulation captures many of the salient features of the ARPES spectra even without taking into account optical matrix element effects. The most well-defined features and clearest dispersion are observed near the zone center, with the mismatched lattice constants of the rotated domains blurring the spectra at higher momentum. Nonetheless, the features from the neighboring zone are still recognizable in the ARPES spectrum Fig. 5(d), as predicted by the simulation in Fig. 5(f). As expected, the features corresponding to the highly dispersive direction along the Sb–Sb chains (shown in blue) are dominant with a lesser contribution from the flatter bands (shown in green) from paths perpendicular to the chains.

The presence of measurable momentum-resolved features in the ARPES spectra further evidences the high degree of surface order that can be achieved in this system, despite the macroscopic rotational disorder in the films. Additionally, the agreement between the measured spectra and calculated electronic structure from the monoclinic phase further corroborates that the phase of the films is predominantly CsSb rather than another member of the Cs–Sb phase diagram. We note, however, that due to the very similar structure of the Sb–Sb chains in the α and β phases, the general dispersive features of α - and β -CsSb are expected to be quite similar. Hence, while the measured dispersive features and DOS match well with calculations for β -CsSb, it is not possible to unequivocally rule out the presence of the α phase with photoemission measurements alone. However, the valence band structure and dispersion observed in these measurements allow Cs₃Sb and Sb metal to be confidently excluded as the dominant photoemitting phases of the film.

VI. QUANTUM EFFICIENCY AND OXIDATION

We finish with a discussion of the low-energy photoemission properties of CsSb, which are of primary importance to its application as a high-brightness photoemitter. To this end, the spectral response of two CsSb films was measured, and the results are summarized in Fig. 6(a), together with the measurement of a codeposited Cs₃Sb reference sample. The films were synthesized on 3C–SiC (100) in a different MBE growth system than those discussed in previous sections; however, the structure was again monitored using *operando* RHEED and the growth temperatures were adjusted to take into account a different thermocouple and heater geometry. The resulting CsSb films exhibited the same fiber texture RHEED pattern observed in Figs. 1(d) and 1(e) and similar QEs of $\sim 10^{-4}$ at 504 nm. Following growth, the samples were transferred *in vacuo* to a storage chamber (to avoid reaction with residual Cs vapor in the growth chamber), where the spectral response was measured between 700 and 400 nm. The maximum QE observed in this range was $\sim 1.2\%$ at 400 nm, which is comparable to Cs₃Sb at 590 nm. The photoemission threshold for each cathode was estimated using the Dowell–Schmerge model⁴⁷ modified for semiconductors. From this fitting, the threshold was estimated to be 2.19 eV for CsSb and 1.65 eV for Cs₃Sb. A threshold of 2.19 eV corresponds to about 566 nm, which is a close to second harmonic of common laser gain media, including Nd:YAG, Nd:YVO₄, and Nd:YAP. This would allow for near-threshold emission, at which

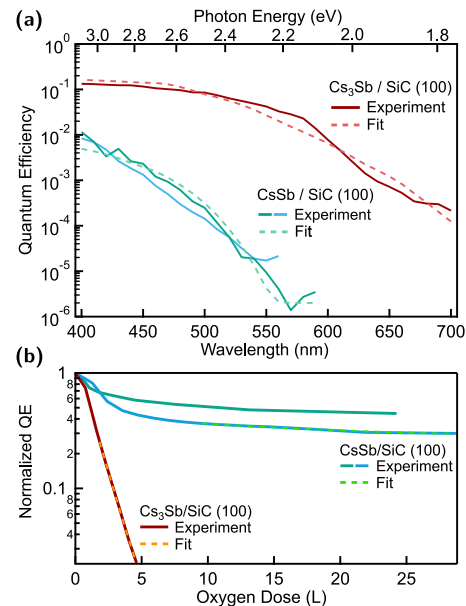


FIG. 6. (a) Spectral response of CsSb and Cs₃Sb thin films grown by codeposition; the film thicknesses are estimated to be 8 nm (blue) and 18 nm (green) for the CsSb films and 45 nm for the Cs₃Sb film (red). Fitting of the response curves gives photoemission thresholds of ~ 566 nm and >650 nm for CsSb and Cs₃Sb, respectively. (b) QE of the same CsSb and Cs₃Sb films as a function of oxygen exposure. Dashed lines represent the best fit to an exponential decay; the ratio between the CsSb and Cs₃Sb decay constants shown is 15.

the beam mean transverse energy is typically minimized,⁹ without the use of complex optical schemes, such as optical parametric amplification.

Following spectral response measurements, the QE degradation of these CsSb photocathodes was measured as a function of oxygen exposure. The samples were exposed to controlled levels of O₂ via a leak valve and nozzle with the O₂ partial pressure maintained between 5×10^{-9} and 5×10^{-8} Torr; the chamber background pressure was below 10^{-9} Torr. The QE is reported as a function of nominal oxygen dose (in Langmuir, 1 L equivalent to 1×10^{-6} Torr \times 1 s) in Fig. 6(b). As a control, a high efficiency Cs₃Sb cathode was also synthesized in the same MBE growth system and dosed in an identical geometry for a comparable reference. Laser wavelengths of 400 and 532 nm were chosen to measure the QE of the CsSb and Cs₃Sb samples, respectively. These wavelengths give similar excess energies ($h\nu - \phi$) for the two phases (0.87 eV for CsSb and 0.68 eV for Cs₃Sb) as well as comparable starting QEs of $\sim 1\%$.

Measuring the QE degradation of the two distinct photocathode films starting from percent-level quantum efficiencies demonstrates the critical difference between CsSb and Cs₃Sb. The CsSb films exhibit a resistance to oxidation more than 10 times that of Cs₃Sb up to an exposure of 30 L. Such chemical stability means that the use of CsSb might extend the usable lifetime of alkali antimonide cathodes in photoguns by over an order of magnitude—extending their use to weeks or months instead of the days-long lifetimes of standard alkali antimonide photoemitters.⁴⁸

VII. CONCLUSIONS

We have demonstrated the synthesis of atomically smooth thin films of CsSb by codeposition of Cs and Sb on both 3C-SiC (100) and graphene/TiO₂ (110). This compound, although less efficient than Cs₃Sb, is characterized by 1% QE at 400 nm, and its photoemission threshold is close to 532 nm; both wavelengths are easily achievable from common laser gain media. This means that it would be equally easy to operate this cathode both at ~1% QE and near the photoemission threshold, where the lowest emittance is expected. Note that the intrinsic emittance has been measured to be minimal at the photoemission threshold only on metal and alkali antimonide photocathodes,¹³ while Cs₂Te is a notable exception,⁴⁹ so further studies are needed to ascertain its photon energy dependence for CsSb. STM and RHEED studies of the morphology indicate that CsSb can be grown atomically smooth via codeposition at a single temperature, which sidesteps some of the challenges facing the growth of AA₂Sb photoemitters, where physical and chemical roughness limit the realization of the intrinsic emittances of the material. We have shown that, despite the random in-plane orientation of domains in the film, the surface remains sufficiently ordered to display dispersion in ARPES. Finally, we observe that CsSb has a greatly improved resistance against oxidation over Cs₃Sb. This allows for the preservation of the atomically ordered surface during vacuum suitcase transfers, as revealed by STM and XPS. This robustness would facilitate studies on the intrinsic emittance of ordered high efficiency semiconductors, providing a benchmark for the theoretical study of low-energy photoemission process on this class of materials. The superior resistance to oxidation, reasonably high quantum efficiency in the visible range, and exceptionally low surface roughness indicate that CsSb is worth considering as a photocathode for future photoinjector beamlines and light sources.

VIII. MATERIALS AND METHODS

A. Thin film synthesis

Cs_xSb thin films were grown on 10 × 10 mm² 3C-SiC (001) and graphene coated rutile TiO₂(110) substrates affixed to custom niobium sample holders in a Veeco Gen10 MBE system ($P_{base} \sim 3 \times 10^{-9}$ Torr) at the PARADIM thin film facility (<https://www.paradim.org/>). Substrates were heated using a resistive heater and the temperature monitored via a thermocouple suspended behind the sample holder. Preceding growth, substrates were degassed at 650 °C for 15 minutes until a clear RHEED pattern was observed and then cooled in vacuum to the deposition temperature. Deposition was performed using molecular beams from an elemental Sb source and a Cs-In alloy source.^{19,50} Typical source temperatures were 288–310 and 407–420 C, giving fluxes of $1.6\text{--}3.0 \times 10^{13}$ and $3.8\text{--}4.9 \times 10^{12}$ for cesium and antimony, respectively. The ratio between the Cs and Sb fluxes was kept between 6 and 6.6 for all growths. Source fluxes were calibrated via quartz crystal microbalance, with an accuracy of ±15%, and the sample thicknesses were estimated using the measured Sb flux as well as the lattice constants and calculated number density of Sb atoms in each phase.

B. Sample characterization

Following growth, samples were transferred through a UHV manifold ($P < 2 \times 10^{-9}$ Torr) to adjacent measurement chambers. The QE was measured using laser diodes, a positively biased collection coil, and a picoammeter. *In situ* ARPES measurements were performed at room temperature in an analysis chamber with base pressure better than 5×10^{-11} Torr using a Scienta Omicron DA30-L electron analyzer and a Fermion Instruments BL1200s plasma discharge lamp generating helium-I ($h\nu = 21.2$ eV) and krypton-I ($h\nu = 10.0$ eV) light. *In situ* x-ray photoelectron spectroscopy (XPS) measurements were performed in the same chamber using a non-monochromated Scienta Omicron DSX400 x-ray source. Selected samples were transferred using a UHV suitcase ($P < 5 \times 10^{-10}$ Torr) to a separate UHV system for further XPS and STM measurements. X-ray photoelectron spectra were analyzed with an Omicron Sphera II analyzer after excitation by an unmonochromated Mg K α source (Omicron DAR 400). XPS spectra were collected at photoelectron emission angles of 0° and 70° from the sample's surface normal. In the latter configuration, the reduced photoelectron escape depth (by ~1/3) enhances the surface sensitivity, making the measurement sensitive to composition gradients and surface contaminants. STM analysis was performed at room temperature in ultrahigh vacuum using a W tip and a Omicron variable-temperature STM. The tunneling conditions were 50–100 pA at –0.5 to –0.8 V applied to the sample.

C. Spectral response and oxygen dosing

For the QE measurements and oxidation experiments depicted in Fig. 6, sample growth on 3C-SiC (100) substrates was reproduced in a custom-built MBE system equipped with *operando* RHEED and QE measurement capabilities. The 3C-SiC (100) substrates were annealed at 650 °C for 1 h before lowering to a temperature between 160 and 200 °C for deposition. Following growth, the samples were moved to an adjacent UHV chamber ($P \sim 10^{-10}$ Torr) to prevent further reaction with residual alkali metal vapor in the growth system. There, the spectral response of the samples was measured using an Oriel Apex Monochromator light source, a Newport optical powermeter (model 843-R), and an SRS 8340 lock-in amplifier. The photocurrent was collected by biasing a metallic coil placed 5 cm from the sample at +120 V.

For the oxygen dosing experiments, selected samples were returned to the growth chamber, where oxygen was introduced from a leak valve through a nozzle directed at the sample surface; the oxygen partial pressure was measured by using a residual gas analyzer. The QE was measured at a single wavelength, provided by a laser diode, and the photocurrent was measured by monitoring the drain current from the electrically floating sample holder (biased at –40 V). Dosing experiments were performed on both CsSb and Cs₃Sb samples in the same configuration to rule out differences between the measured pressure at the gauge and the pressure at the sample surface arising to the chamber's pumping layout. The QE vs oxygen dose curves have been fitted with a simple exponential decay. In particular, for the CsSb data, the initial faster decay within the first 10 L, visible in Fig. 6(b), was disregarded. The ratio between the decay constants of CsSb and Cs₃Sb is found to be ~7 – 15.

D. Density functional theory calculations

Plane-wave density functional theory calculations of α - and β -CsSb were performed using GGA-PBE exchange–correlation functionals⁵¹ and SG15 norm-conserving pseudopotentials⁵² implemented in JDFTx.⁵³ For the monoclinic (β -CsSb) structure, a plane wave cutoff of 40 hartrees was used and optimized structural parameters of $a = 15.50 \text{ \AA}$, $b = 7.50 \text{ \AA}$, $c = 14.55 \text{ \AA}$, and $\beta = 113.82^\circ$ were obtained from a relaxation calculation; calculations of total ground state energy and DOS used a mesh of $5 \times 7 \times 5$. To enable efficient interpolation of the electronic band structures to arbitrary crystal momenta and for more accurate calculation of the DOS, the Wannier interpolation technique⁵⁴ was used to generate a maximally localized Wannier basis set⁵⁵ using a supercell of $4 \times 7 \times 4$ primitive cells using linear combinations of bulk Bloch bands at binding energies from 0 to 11 eV below the valence band maximum. To generate the simulated ARPES spectra in Figs. 5(e)–5(f), a set of spectral functions $A(\mathbf{k}, \omega) \sim 1/((\omega - \varepsilon_{i,\mathbf{k}})^2 + \Sigma''^2)$ was then generated from the Wannier interpolated eigenvalues, $\varepsilon_{i,\mathbf{k}}$, and an imaginary self-energy of $\Sigma'' = 75 \text{ meV}$.

SUPPLEMENTARY MATERIAL

See the supplementary material for additional RHEED and STM images, further display and analysis of XPS data, and a discussion of the crystal and electronic structure of the orthorhombic phase α -CsSb.

ACKNOWLEDGMENTS

This work was supported by the U.S. National Science Foundation under Grant No. PHY-1549132, the Center for Bright Beams, and the National Science Foundation [Platform for the Accelerated Realization, Analysis, and Discovery of Interface Materials (PARADIM)] under Cooperative Agreement No. DMR-2039380. Work by C.T.P. and K.M.S. also acknowledges support from the NSF under Grant Nos. DMR-2104427 and AFOSR FA9550-21-1-0168. J.M.M. acknowledges support from DOE under Grant Nos. DE-AC02-76SF00515 and DE-SC0020144. This work made use of the Cornell Center for Materials Research Facilities supported by the National Science Foundation under Award No. DMR-1719875. Substrate preparation was performed, in part, at the Cornell NanoScale Facility, a member of the National Nanotechnology Coordinated Infrastructure (NNCI), which is supported by the National Science Foundation (Grant No. NNCI-2025233). Electronic structure calculations were carried out, in part, at the Advanced Research Computing at Hopkins (ARCH) core facility (rockfish.jhu.edu), which is supported by the National Science Foundation (NSF) under Grant No. OAC 1920103. The authors thank Sean C. Palmer for his assistance in substrate preparation and Betül Pamuk for her assistance in utilizing the high-performance computing resources.

AUTHOR DECLARATIONS

Conflict of Interest

The authors have no conflicts to disclose.

Author Contributions

Sample synthesis was performed by A.G., C.T.P., C.A.P., E.E., and W.J.D. under the supervision of J.M.M., K.M.S., and D.G.S. with assistance from H.P. QE experiments were performed by A.G., C.A.P., E.E., and C.T.P. C.T.P. and B.D.F. performed the *in situ* ARPES and XPS measurements with assistance from L.M. and C.H. and data was analyzed by C.T.P. and V.A. STM and angle-dependent XPS measurements were performed by J.B. and W.J.D., and A.G. performed quantitative XPS data analysis under the supervision of M.A.H. DFT calculations were performed by C.T.P. and J.K.N. under the supervision of K.M.S. and T.A.A., A.G., C.T.P., C.A.P. and J.M.M. prepared the manuscript with input from all authors.

C. T. Parzyck: Conceptualization (equal); Formal analysis (equal); Investigation (equal); Writing – original draft (equal). **C. A. Pennington:** Formal analysis (equal); Investigation (equal); Writing – original draft (equal). **W. J. I. DeBenedetti:** Formal analysis (equal); Investigation (equal); Writing – review & editing (equal). **J. Balajka:** Formal analysis (equal); Investigation (equal); Writing – review & editing (equal). **E. M. Echeverria:** Formal analysis (equal); Investigation (equal); Writing – review & editing (equal). **H. Paik:** Investigation (supporting); Resources (equal); Writing – review & editing (equal). **L. Moreschini:** Investigation (supporting); Resources (equal); Writing – review & editing (equal). **B. D. Faeth:** Investigation (supporting); Resources (equal); Writing – review & editing (equal). **C. Hu:** Investigation (supporting); Resources (equal); Writing – review & editing (equal). **J. K. Nangoi:** Formal analysis (supporting); Investigation (supporting); Resources (equal); Writing – review & editing (equal). **V. Anil:** Formal analysis (supporting); Writing – review & editing (equal). **T. A. Arias:** Formal analysis (supporting); Supervision (supporting); Writing – review & editing (equal). **M. A. Hines:** Formal analysis (equal); Resources (equal); Supervision (equal); Writing – review & editing (equal). **D. G. Schlom:** Resources (equal); Supervision (equal); Writing – review & editing (equal). **A. Galdi:** Conceptualization (equal); Formal analysis (equal); Investigation (equal); Supervision (equal); Writing – original draft (equal). **K. M. Shen:** Conceptualization (equal); Supervision (equal); Writing – review & editing (equal). **J. M. Maxson:** Conceptualization (equal); Supervision (equal); Writing – original draft (equal).

DATA AVAILABILITY

The data that support the findings of this study are available within the article and its supplementary material. Additional data related to the growth and structural characterization are available at DOI [10.34863/leg8-ak52](https://doi.org/10.34863/leg8-ak52). Additional data connected to the study are available from the corresponding author upon reasonable request.

REFERENCES

- 1 M. Scholz, “FEL performance achieved at European XFEL,” Proceedings of the 9th International Particle Accelerator Conference IPAC2018, Canada, 2018.
- 2 P. Emma, R. Akre, J. Arthur, R. Bionta, C. Bostedt, J. Bozek, A. Brachmann, P. Bucksbaum, R. Coffee, F.-J. Decker, Y. Ding, D. Dowell, S. Edstrom, A. Fisher, J. Frisch, S. Gilevich, J. Hastings, G. Hays, P. Hering, Z. Huang, R. Iverson, H. Loos, M. Messerschmidt, A. Miahnahri, S. Moeller, H.-D. Nuhn, G. Pile, D. Ratner,

- J. Rzepiela, D. Schultz, T. Smith, P. Stefan, H. Tompkins, J. Turner, J. Welch, W. White, J. Wu, G. Yocky, and J. Galayda, "First lasing and operation of an Angstrom-wavelength free-electron laser," *Nat. Photonics* **4**, 641–647 (2010).
- ³V. A. Lobastov, R. Srinivasan, and A. H. Zewail, "Four-dimensional ultrafast electron microscopy," *Proc. Natl. Acad. Sci.* **102**, 7069–7073 (2005).
- ⁴G. Sciaini and R. J. D. Miller, "Femtosecond electron diffraction: Heralding the era of atomically resolved dynamics," *Rep. Prog. Phys.* **74**, 096101 (2011).
- ⁵W. H. Li, C. J. R. Duncan, M. B. Andorf, A. C. Bartnik, E. Bianco, L. Cultrera, A. Galdi, M. Gordon, M. Kaemingk, C. A. Pennington, L. F. Kourkoutis, I. V. Bazarov, and J. M. Maxson, "A kiloelectron-volt ultrafast electron microdiffraction apparatus using low emittance semiconductor photocathodes," *Struct. Dyn.* **9**, 024302 (2022).
- ⁶S. Michizono, "The international linear collider," *Nat. Rev. Phys.* **1**, 244–245 (2019).
- ⁷V. N. Litvinenko and Y. S. Derbenev, "Coherent electron cooling," *Phys. Rev. Lett.* **102**, 114801 (2009).
- ⁸M. Bai, T. Barklow, R. Bartoldus, M. Breidenbach, P. Grenier, Z. Huang, M. Kagan, J. Wellen, Z. Li, T. W. Markiewicz, E. A. Nanni, M. Nasr, C.-K. Ng, M. Oriunno, M. E. Peskin, T. G. Rizzo, J. Rosenzweig, A. G. Schwartzman, V. Shiltsev, E. Simakov, B. Sapatro, D. Su, S. Tantawi, C. Vernieri, G. White, and C. C. Young, "C3: A 'cool' route to the Higgs boson and beyond," [arXiv:2110.15800](https://arxiv.org/abs/2110.15800) [hep-ex] (2021)
- ⁹J. Maxson, L. Cultrera, C. Gulliford, and I. Bazarov, "Measurement of the tradeoff between intrinsic emittance and quantum efficiency from a NaKSb photocathode near threshold," *Appl. Phys. Lett.* **106**, 234102 (2015).
- ¹⁰G. Gevorkyan, S. Karkare, S. Emamian, I. V. Bazarov, and H. A. Padmore, "Effects of physical and chemical surface roughness on the brightness of electron beams from photocathodes," *Phys. Rev. Accel. Beams* **21**, 093401 (2018).
- ¹¹J. Wellen, D. Filippetto, S. Karkare, J. Maxson, P. Musumeci, J. Smedley, and T. Vecchione, "The quest for the Perfect cathode," JACoW NAPAC2022, TUYD3, <http://www.jacow.org> (2022).
- ¹²A. Sommer, *Photoemissive Materials: Preparation, Properties, and Uses* (Krieger, 1980).
- ¹³L. Cultrera, S. Karkare, H. Lee, X. Liu, I. Bazarov, and B. Dunham, "Cold electron beams from cryocooled, alkali antimonide photocathodes," *Phys. Rev. Spec. Top.-Accel. Beams* **18**, 113401 (2015).
- ¹⁴C. W. Bates, T. M. van Atekum, G. K. Wertheim, D. N. E. Buchanan, and K. E. Clements, "X-ray photoemission studies of superficially oxidized cesium antimonide photoemitters," *Appl. Phys. Lett.* **38**, 387–389 (1981).
- ¹⁵A. Galdi, W. J. I. DeBenedetti, J. Balajka, L. Cultrera, I. V. Bazarov, J. M. Maxson, and M. A. Hines, "The effects of oxygen-induced phase segregation on the interfacial electronic structure and quantum efficiency of Cs₃Sb photocathodes," *J. Chem. Phys.* **153**, 144705 (2020).
- ¹⁶P. Saha, E. Echeverria, A. Galdi, S. Karkare, J. Maxson, E. Montgomery, C. Pennington, and S. Poddar, "Epitaxial alkali-antimonide photocathodes on lattice-matched substrates," JACoW NAPAC2022, TUYD5, <http://www.jacow.org> (2022).
- ¹⁷P. Saha, O. Chubenko, G. S. Gevorkyan, A. Kachwala, C. J. Knill, C. Sarabia-Cardenas, E. Montgomery, S. Poddar, J. T. Paul, R. G. Hennig, H. A. Padmore, and S. Karkare, "Physically and chemically smooth cesium-antimonide photocathodes on single crystal strontium titanate substrates," *Appl. Phys. Lett.* **120**, 194102 (2022).
- ¹⁸A. Galdi, C. T. Parzyck, W. J. I. DeBenedetti, J. Balajka, L. Cultrera, H. Paik, L. Moreschini, C. Hu, K. M. Shen, M. A. Hines, and J. M. Maxson, "Understanding the growth dynamics Cs-Sb thin films via in-situ characterization techniques: Towards epitaxial alkali antimonide photocathodes," Proceedings of IPAC'21, WEPAB157, 2021.
- ¹⁹C. T. Parzyck, A. Galdi, J. K. Nangoi, W. J. I. DeBenedetti, J. Balajka, B. D. Faeth, H. Paik, C. Hu, T. A. Arias, M. A. Hines, D. G. Schlom, K. M. Shen, and J. M. Maxson, "Single-crystal alkali antimonide photocathodes: High efficiency in the ultrathin limit," *Phys. Rev. Lett.* **128**, 114801 (2022).
- ²⁰J. Feng, S. Karkare, J. Nasiatka, S. Schubert, J. Smedley, and H. Padmore, "Near atomically smooth alkali antimonide photocathode thin films," *J. Appl. Phys.* **121**, 044904 (2017).
- ²¹A. Galdi, J. Balajka, W. J. I. DeBenedetti, L. Cultrera, I. V. Bazarov, M. A. Hines, and J. M. Maxson, "Reduction of surface roughness emittance of Cs₃Sb photocathodes grown via codeposition on single crystal substrates," *Appl. Phys. Lett.* **118**, 244101 (2021).
- ²²F. Liu, L. Guo, J. DeFazio, V. Pavlenko, M. Yamamoto, N. A. Moody, and H. Yamaguchi, "Photoemission from bialkali photocathodes through an atomically thin protection layer," *ACS Appl. Mater. Interfaces* **14**, 1710–1717 (2022).
- ²³J. Biswas, M. Gaowei, A. Liu, S. Poddar, L. Stan, J. Smedley, J. T. Sadowski, and X. Tong, "Cesium intercalation of graphene: A 2D protective layer on alkali antimonide photocathode," *APL Mater.* **10**, 111115 (2022).
- ²⁴I. Will and G. Klemz, "Drive lasers for photoinjectors," *Proceedings - 41st Advanced ICFA Beam Dynamics Workshop on Energy Recovery Linacs, ERL 2007* (2007), pp. 1–5, <https://accelconf.web.cern.ch/erl07/papers/H13.pdf>.
- ²⁵A. Galdi, W. J. I. DeBenedetti, J. Balajka, L. Cultrera, M. A. Hines, S. A. McBride, J. B. Baretz, F. Ikponwmen, I. V. Bazarov, and J. M. Maxson, "Towards the optimization of photocathode properties via surface science techniques: A study on Cs₃Sb thin film growth," Proceedings of NAPAC'19, MOPLH24, 2019.
- ²⁶V. Pavlenko, J. Smedley, A. Scheinker, R. L. Fleming, A. Alexander, M. A. Hoffbauer, and N. A. Moody, "Stoichiometry control and automated growth of alkali antimonide photocathode films by molecular beam deposition," *Appl. Phys. Lett.* **120**, 091901 (2022).
- ²⁷R. P. Vinci, *Thin Films: Texture Effects on Mechanical Properties, Encyclopedia of Materials: Science and Technology* (Elsevier, 2001).
- ²⁸I. Martini, E. Chevallay, V. Fedosseev, C. Hessler, H. Neupert, V. Nistor, and M. Taborelli, "X-ray photoemission spectroscopy studies of cesium antimonide photocathodes for photoinjector applications," *Phys. Procedia* **77**, 34–41 (2015).
- ²⁹J. F. Moulder, W. F. Stickle, P. E. Sobol, and K. D. Bomben, *Handbook of X-Ray Photoelectron Spectroscopy* (Perkin-Elmer Corporation, 1992).
- ³⁰L. Soriano and L. Galán, "Interaction of cesium-potassium antimonide photocathode materials with oxygen: An X-ray photoelectron spectroscopy study," *Jpn. J. Appl. Phys.* **32**, 4737–4744 (1993).
- ³¹C. Cocchi, S. Mistry, M. Schmeißer, R. Amador, J. Kühn, and T. Kamps, "Electronic structure and core electron fingerprints of caesium-based multi-alkali antimonides for ultra-bright electron sources," *Sci. Rep.* **9**, 18276 (2019).
- ³²M. A. Schmeißer, S. Mistry, H. Kirschner, S. Schubert, A. Jankowiak, T. Kamps, and J. Kühn, "Towards the operation of Cs-K-Sb photocathodes in superconducting RF photoinjectors," *Phys. Rev. Accel. Beams* **21**, 113401 (2018).
- ³³G. Ebbinghaus and A. Simon, "Electronics structures of Rb, Cs and some of their metallic oxides studied by photoelectron spectroscopy," *Chem. Phys.* **43**, 117–133 (1979).
- ³⁴N. G. Krishnan, W. N. Delgass, and W. D. Robertson, "Electron binding energies of core levels in caesium adsorbed on a nickel (100) surface," *J. Phys. F: Met. Phys.* **7**, 2623–2635 (1977).
- ³⁵J. Jupille, P. Dolle, and M. Besançon, "Ionic oxygen species formed in the presence of lithium, potassium and cesium," *Surf. Sci.* **260**, 271–285 (1992).
- ³⁶W. K. Liu, W. T. Yuen, and R. A. Stradling, "Preparation of InSb substrates for molecular beam epitaxy," *J. Vac. Sci. Technol., B* **13**, 1539–1545 (1995).
- ³⁷C. Morant, L. Galán, and J. M. Sanz, "An XPS study of the initial stages of oxidation of hafnium," *Surf. Interface Anal.* **16**, 304–308 (1990).
- ³⁸Y. Sun, Z. Liu, P. Pianetta, and D.-I. Lee, "Formation of cesium peroxide and cesium superoxide on InP photocathode activated by cesium and oxygen," *J. Appl. Phys.* **102**, 074908 (2007).
- ³⁹S. Karkare and I. Bazarov, "Effect of nanoscale surface roughness on transverse energy spread from GaAs photocathodes," *Appl. Phys. Lett.* **98**, 094104 (2011).
- ⁴⁰H. Georg von Schnering, W. Hönle, and G. Rrogull, "Die monoantimonide RbSb und CsSb/the monoantimonides RbSb and CsSb," *Z. Naturforsch., B: J. Chem. Sci.* **34**, 1678–1682 (1979).
- ⁴¹F. Emmerling, C. Hirschle, and C. Röhr, "Cs₃Sb₈ und β-CsSb: Zwei neue binäre Zintl-Phasen," *Z. Anorg. Allg. Chem.* **628**, 559–563 (2002).
- ⁴²K. Momma and F. Izumi, "VESTA 3 for three-dimensional visualization of crystal, volumetric and morphology data," *J. Appl. Crystallogr.* **44**, 1272–1276 (2011).
- ⁴³Y. Hinuma, G. Pizzi, Y. Kumagai, F. Oba, and I. Tanaka, "Band structure diagram paths based on crystallography," *Comput. Mater. Sci.* **128**, 140–184 (2017).

- ⁴⁴A. Togo and I. Tanaka, Spglib: A software library for crystal symmetry search, 2018.
- ⁴⁵J. Yeh and I. Lindau, "Atomic subshell photoionization cross sections and asymmetry parameters: $1 \leq Z \leq 103$," *At. Data Nucl. Data Tables* **32**, 1–155 (1985).
- ⁴⁶A. Damascelli, "Probing the electronic structure of complex systems by ARPES," *Phys. Scr.* **T109**, 61–74 (2004).
- ⁴⁷D. H. Dowell and J. F. Schmerge, "Quantum efficiency and thermal emittance of metal photocathodes," *Phys. Rev. Spec. Top.–Accel. Beams* **12**, 074201 (2009).
- ⁴⁸L. Cultrera, S. Karkare, B. Lillard, A. Bartnik, I. Bazarov, B. Dunham, W. Schaff, and K. Smolenski, "Growth and characterization of rugged sodium potassium antimonide photocathodes for high brilliance photoinjector," *Appl. Phys. Lett.* **103**, 103504 (2013).
- ⁴⁹C. M. Pierce, J. K. Bae, A. Galdi, L. Cultrera, I. Bazarov, and J. Maxson, "Beam brightness from Cs–Te near the photoemission threshold," *Appl. Phys. Lett.* **118**(12), 124101 (2021).
- ⁵⁰D. Du, P. J. Strohbeen, H. Paik, C. Zhang, K. T. Genser, K. M. Rabe, P. M. Voyles, D. G. Schlom, and J. K. Kawasaki, "Control of polymorphism during epitaxial growth of hyperferroelectric candidate LiZnSb on GaSb (111)B," *J. Vac. Sci. Technol., B* **38**, 22208 (2020).
- ⁵¹J. P. Perdew, K. Burke, and M. Ernzerhof, "Generalized gradient approximation made simple," *Phys. Rev. Lett.* **77**, 3865–3868 (1996).
- ⁵²M. Schlipf and F. Gygi, "Optimization algorithm for the generation of ONCV pseudopotentials," *Comput. Phys. Commun.* **196**, 36–44 (2015).
- ⁵³R. Sundararaman, K. Letchworth-Weaver, K. A. Schwarz, D. Gunceler, Y. Ozhables, and T. Arias, "JDFTx: Software for joint density-functional theory," *SoftwareX* **6**, 278–284 (2017).
- ⁵⁴N. Marzari, A. A. Mostofi, J. R. Yates, I. Souza, and D. Vanderbilt, "Maximally localized Wannier functions: Theory and applications," *Rev. Mod. Phys.* **84**, 1419–1475 (2012).
- ⁵⁵N. Marzari and D. Vanderbilt, "Maximally localized generalized Wannier functions for composite energy bands," *Phys. Rev. B* **56**, 12847–12865 (1997).

Supplementary Materials for: Atomically smooth films of CsSb: a chemically robust visible light photocathode

Christopher T. Parzyck,¹ Chad A. Pennington,² William J. I. DeBenedetti,³ Jan Balajka,³ Elena Echeverria,² Hanjong Paik,^{4, 5, 6} Luca Moreschini,⁴ Brendan D. Faeth,⁴ Cheng Hu,⁴ Johannes K. Nangoi,¹ Vivek Anil,¹ Tomas A. Arias,¹ Melissa A. Hines,³ Darrell G. Schlom,^{7, 8, 9} Alice Galdi*,^{2, 10} Kyle M. Shen,^{1, 8} and Jared M. Maxson*²

¹Laboratory of Atomic and Solid State Physics, Department of Physics, Cornell University, Ithaca, NY 14853, USA

²Cornell Laboratory for Accelerator-Based Sciences and Education, Cornell University, Ithaca, NY 14853, USA

³Department of Chemistry and Chemical Biology, Cornell University, Ithaca, NY 14853, USA

⁴Platform for the Accelerated Realization, Analysis,

and Discovery of Interface Materials (PARADIM), Cornell University, Ithaca, NY 14853, USA

⁵School of Electrical & Computer Engineering, University of Oklahoma, Norman, Oklahoma 73019

⁶Center for Quantum Research and Technology, University of Oklahoma, Norman, Oklahoma 73019

⁷Department of Materials Science and Engineering, Cornell University, Ithaca, NY 14853, USA

⁸Kavli Institute at Cornell for Nanoscale Science, Cornell University, Ithaca, NY 14853, USA

⁹Leibniz-Institut für Kristallzüchtung, Max-Born-Straße 2, 12489 Berlin, Germany

¹⁰Department of Industrial Engineering, University of Salerno, Fisciano (SA) 84084, Italy

(Dated: July 2, 2023)

*Authors to whom correspondence should be addressed: agaldi@unisa.it, jmm586@cornell.edu

CONTENTS

RHEED	2
Additional XPS/UPS spectra and Auger parameter analysis	3
Morphology and Crystal Structure	4
Additional DFT Calculations	8
Work function Estimates	9
References	9

RHEED

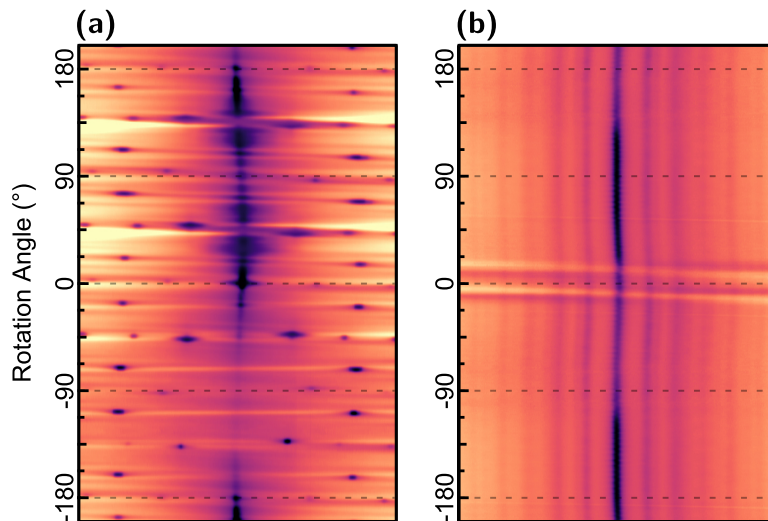


FIG. S1. Map of the RHEED intensity profile as a function of the azimuthal incidence angle, showing the in-plane 4-fold periodicity of the 3C-SiC (100) substrate (a) and lack of thereof for a typical CsSb film (b).

The in-plane periodicity of the crystal structure of the films can be determined by measuring the intensity profile of the RHEED pattern while rotating the sample along its surface normal. As expected for a cubic crystal, the pattern of the 3C-SiC (100) substrate repeats itself every 90° , as shown in the map in the left panel of Figure S1. The intensity map measured for a typical CsSb sample (right panel of Figure S1), on the other hand, does not show any periodicity as a function of the rotation angle, but a rather uniform intensity profile. This indicates that, while the surface is flat and produces a 2D diffraction pattern, there is lack of ordering of the in-plane lattice vectors. This type of crystal texture, with a well defined out-of-plane lattice parameter and random orientation of the in-plane lattice vectors, is called “fiber texture” [1].

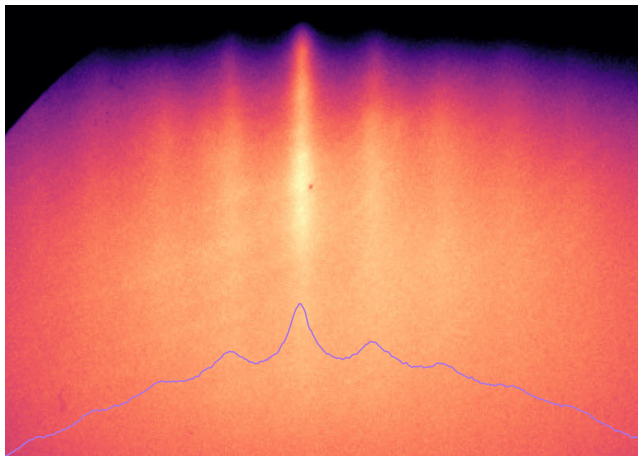


FIG. S2. Typical RHEED pattern of a sample grown for the oxidation experiments in the PHOEBE deposition system at $T_{sub} = 165^\circ\text{C}$. A line profile of the intensity is superimposed to the image. The color scale uses logarithmic mapping.

For the spectral response and oxygen dosing experiments, shown in Fig. 6 of the main text, sample growth was reproduced in a custom built MBE system at the PHOEBE (photocathode epitaxy and beam experiments) laboratory, Cornell University. *In operando* RHEED was used to assess the structure and phase of the resulting films and in a growth regime of $160\text{-}200^\circ\text{C}$ an identical azimuthal RHEED pattern to those presented in Fig. 1(d) and (e). The observed shift in the growth window is attributable to differences in the heater and thermocouple design between the two systems, which results in a different tooling factor between the measured thermocouple temperature and the

sample surface temperature. Pressures were maintained below 2×10^{-8} Torr in the MBE chamber during deposition, while the base pressure of the system is $1.3 - 3 \times 10^{-10}$ Torr.

ADDITIONAL XPS/UPS SPECTRA AND AUGER PARAMETER ANALYSIS

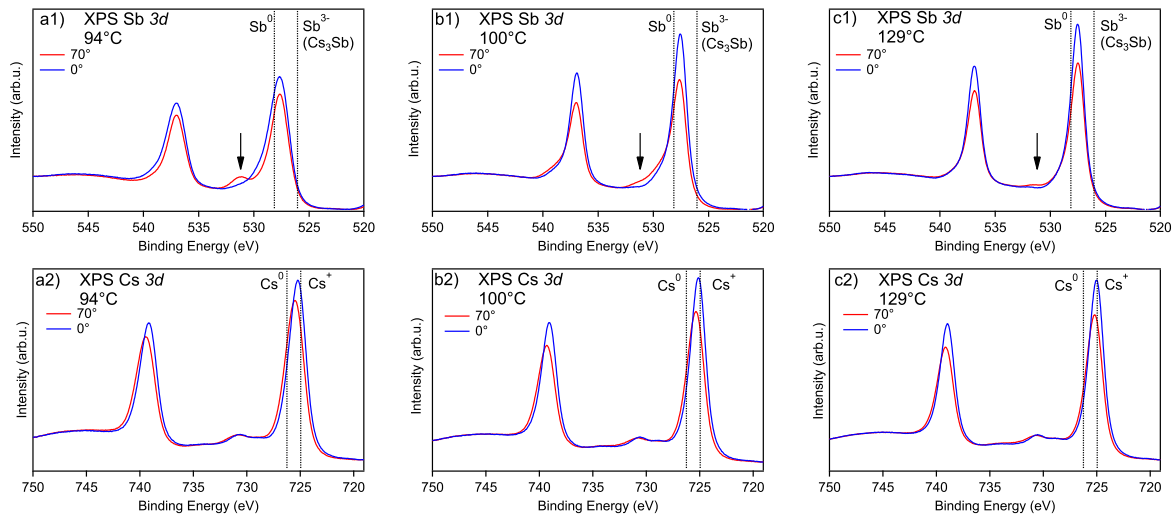


FIG. S3. Sb $3d$ (top row) and Cs $3d$ (bottom row) XPS spectra of CsSb samples grown at $T_{sub} = 94^\circ\text{C}$ (a1,a2), $T_{sub} = 100^\circ\text{C}$ (b1,b2), $T_{sub} = 129^\circ\text{C}$ (c1,c2). Red lines represent the spectra measured at grazing emission (70° from surface normal), while blue lines represent the spectra measured in normal emission (0°). All spectra are normalized so that the background coincides above and below the emission peaks. Dotted lines represent the reference energies for the $3d_{5/2}$ binding energy of different valence states of Sb and Cs, [2–4] while the arrow indicates the oxygen associated peak at 531.2 eV.

In Figure S3 we compare the XPS spectra shown in the main text, collected at 70° from surface normal, with the measurement collected with normal emission (less surface sensitive). The oxygen peak is enhanced in the grazing emission measurements, while is near the detection limit in the normal emission measurements. The Cs $3d_{5/2}$ binding energy shifts towards higher binding energy in grazing emission. These observations are consistent with a surface Cs-O layer and with the associated band bending, already observed in superficially oxidized Cs_3Sb films. [5] Compared to the Cs_3Sb case, the composition of the samples appears homogeneous, with a single Sb oxidation state of 1-. We attribute the Cs-O oxide layer to oxidation of excess Cs deposited on the sample surface, which is more abundant in the samples grown at lower substrate temperature, rather than phase segregation induced by oxygen exposure as observed for Cs_3Sb and other Sb^{3-} compounds [4–6]. In Figure S4, we report the measured Auger parameter of the CsSb samples. In particular, the Sb Auger parameter is significantly different than the one of metal Sb.

In Figure S5 we report *in situ* XPS spectra taken at a 30° off-normal emission angle using a non-monochromatic Al- α source ($h\nu = 1486.3$ eV) in the ARPES measurement chamber on the same UHV manifold as the growth system. The Cs $3d$ and Sb $3d$ spectra reported in panels (b) and (c) do not differ substantially from those taken following the vacuum suitcase transfer or from samples grown on Graphene coated TiO_2 (110) – indicating that the stoichiometry of both sets of samples is comparable, consistent with structural evidence from RHEED. We note here that the transmission function of the electron analyzer used in this measurement is not well characterized so the peak ratios cannot be as precisely related to the elemental ratios as those reported in the main text but there is still rough agreement between the Cs and Sb peak intensities as expected for CsSb. Figure S5(d) shows the valence band taken by XPS, which agrees well with those measured by UPS, modulo the absence of the O $2p$ peaks which are suppressed by a low cross section at this photon energy [10], indicating the electronic structure measured in Fig. 5 is indeed representative of the film bulk.

In Figure S6(a) the same Sb $3d$ spectrum of Figure S5(c) is compared with the reference spectra of a Cs_3Sb and a Sb film sample grown in the same system and measured immediately after growth. Despite being exposed to the same vacuum environment, the Cs_3Sb sample shows higher oxygen content than the CsSb one, and various different oxide species. This resilience to oxidation of CsSb is also apparent in more surface sensitive low energy photoemission measurements of the valence bands shown in Figure S6(b). In the angle-integrated spectra, the O $2p$ peaks at 5.5 eV

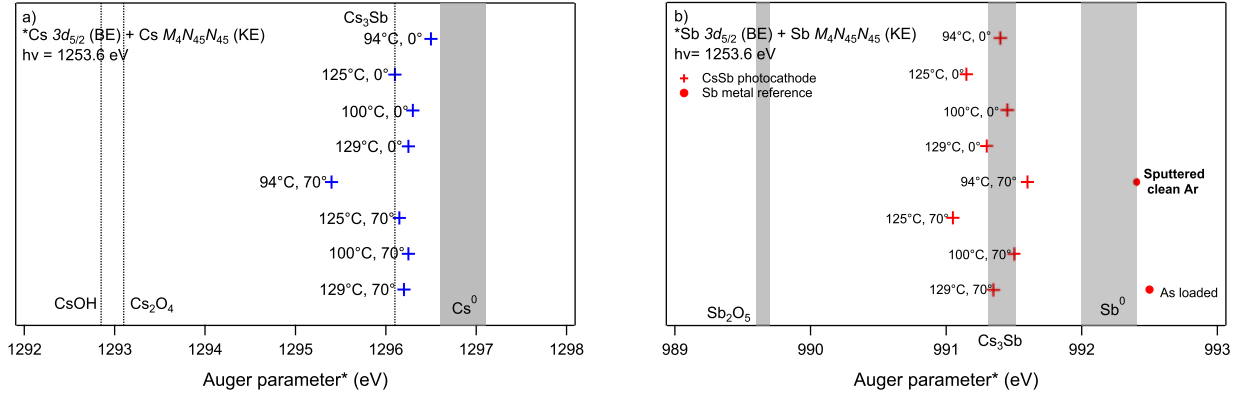


FIG. S4. Auger Parameter for the Cs (a) and the Sb (b) $3d_{5/2}$ peaks of a series of CsSb samples grown at different temperature and for a Sb metal reference [in (b)]. The Auger parameter is compared to literature references of different Sb and Cs compounds, indicated by grey bands or lines. Labels indicate the growth temperature of the samples and the measurement emission angle.

are substantially stronger (compared to the near E_f Sb $5p$ peaks) in the Cs₃Sb samples than in CsSb samples which were exposed to the same vacuum environment.

MORPHOLOGY AND CRYSTAL STRUCTURE

Figure S7 provides additional STM images from the three samples depicted in main text figure 3. We note that in zoomed in images of the sample grown in regime (II) the grains show small terraces on a lateral length scale of ~ 50 nm. As mentioned in the main text, grain boundaries can be observed between rotationally misaligned domains, as depicted in Figure S7(d) where two sets of atomic columns meet at an angle of $\sim 20^\circ$. Figure S8 shows the crystal structure of the orthorhombic α phase of CsSb based on the structural parameters from x-ray refinement of the bulk compound in [11]. In this structure the Sb-Sb spirals all share the same chirality, as shown in panel (b), however the stacking and rotation structure differs slightly from that of the β phase. As a result the spirals are packed slightly closer together and produce a smaller inter-plane spacing along the layered directions of $(002)_{or}$ and $(011)_{or}$. The band structure for this structure is relayed in Figure S9.

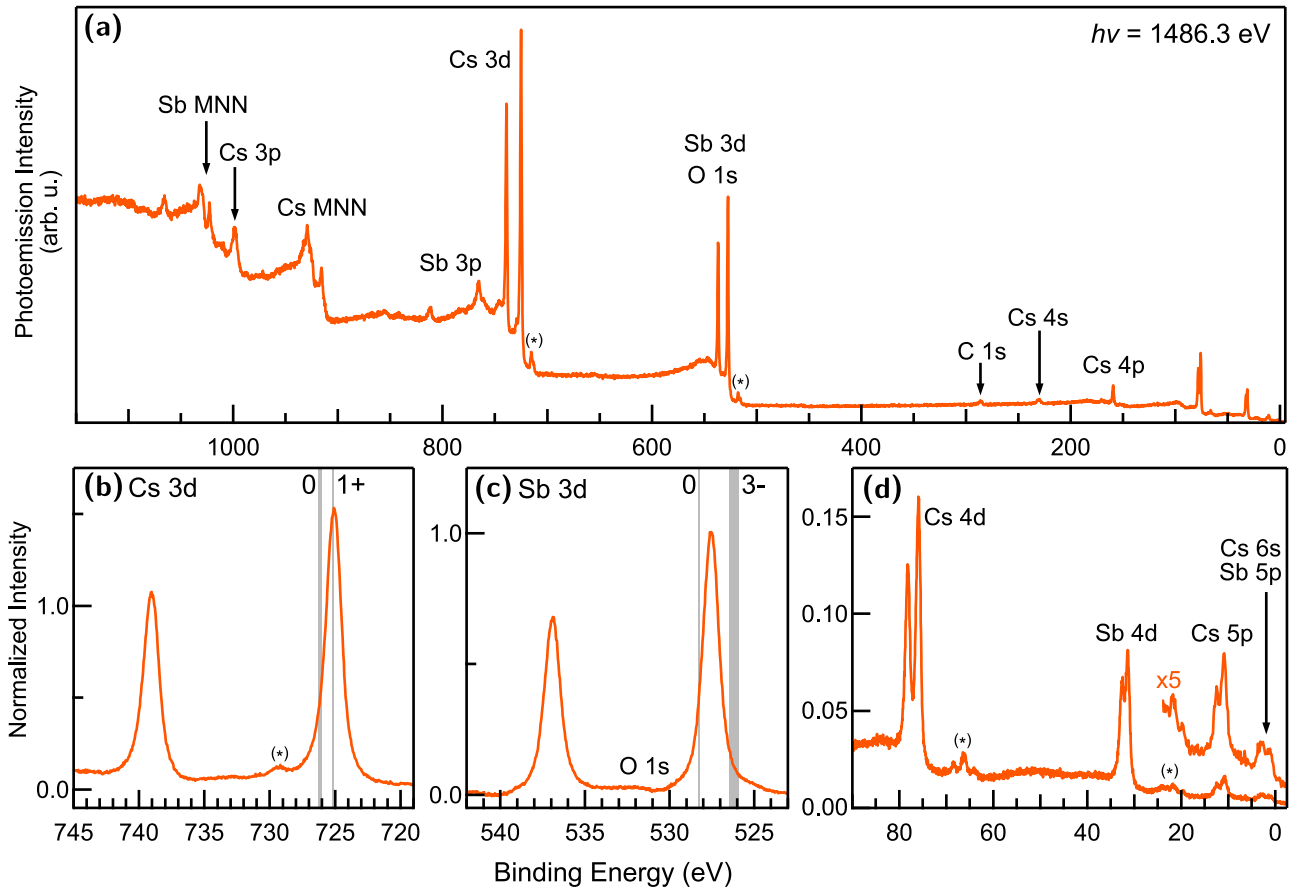


FIG. S5. *In situ* XPS spectra of CsSb / 3C-SiC (100) collected with a non-monochromated Al- $\kappa\alpha$ source; this is the same sample whose ARPES spectrum is reported in Fig. 5(c) of the main text. (a) Survey spectrum; peaks were identified using XPS reference data from 7 and 8. (b) Background subtracted Cs 3d region, references for metallic Cs and Cs¹⁺ are marked in grey. (c) Background subtracted Sb 3d region with references for metallic Sb and Sb³⁻ are marked in grey. No weight from the O 1s peak is visible above the plasmon loss peaks. (d) Valence band region, without background subtraction. Intensities in panels (b-d) are normalized to the Sb 3d_{5/2} peak intensity. Satellite peaks arising from the Al- $\kappa\alpha_3$ line ($E_{k\alpha_1} - E_{k\alpha_3} = 9.7$ eV and $I_{k\alpha_1} : I_{k\alpha_3} = 100 : 7.3$ [9]) line are marked with an asterisk (*).

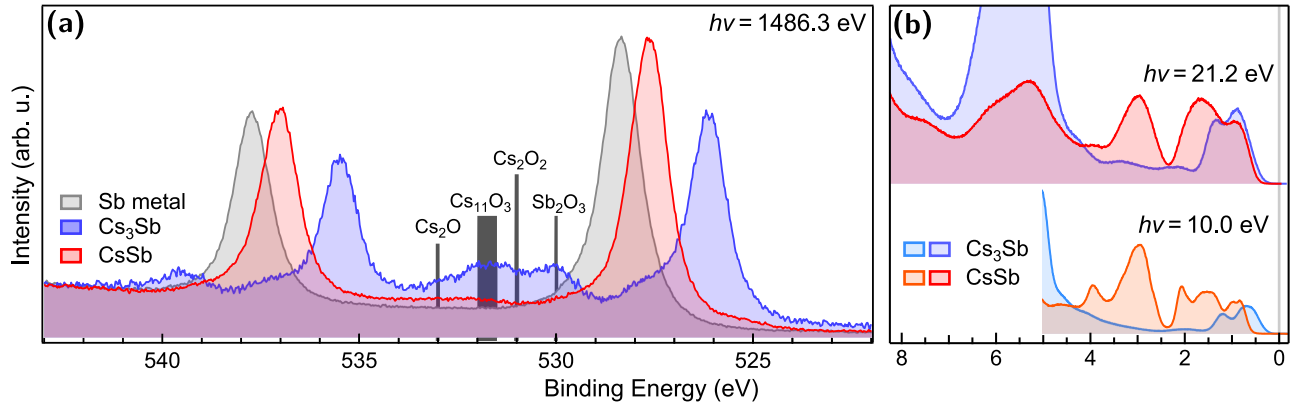


FIG. S6. (a) Sb 3d XPS spectrum of a CsSb sample, compared to Cs₃Sb and Sb reference samples, all measured *in-situ* immediately after growth. Grey bars indicate the O 1s binding energies associated to Cs and Sb oxides. The spectra are normalized so that the background coincides above and below the emission peaks. (b) Angle-integrated ARPES spectra of different Cs₃Sb and CsSb samples measured using photon energies of 21.2 and 10.0 eV. The samples shown were measured *in situ* following sample growth with similar levels of exposure to residual gasses in the transfer chamber.

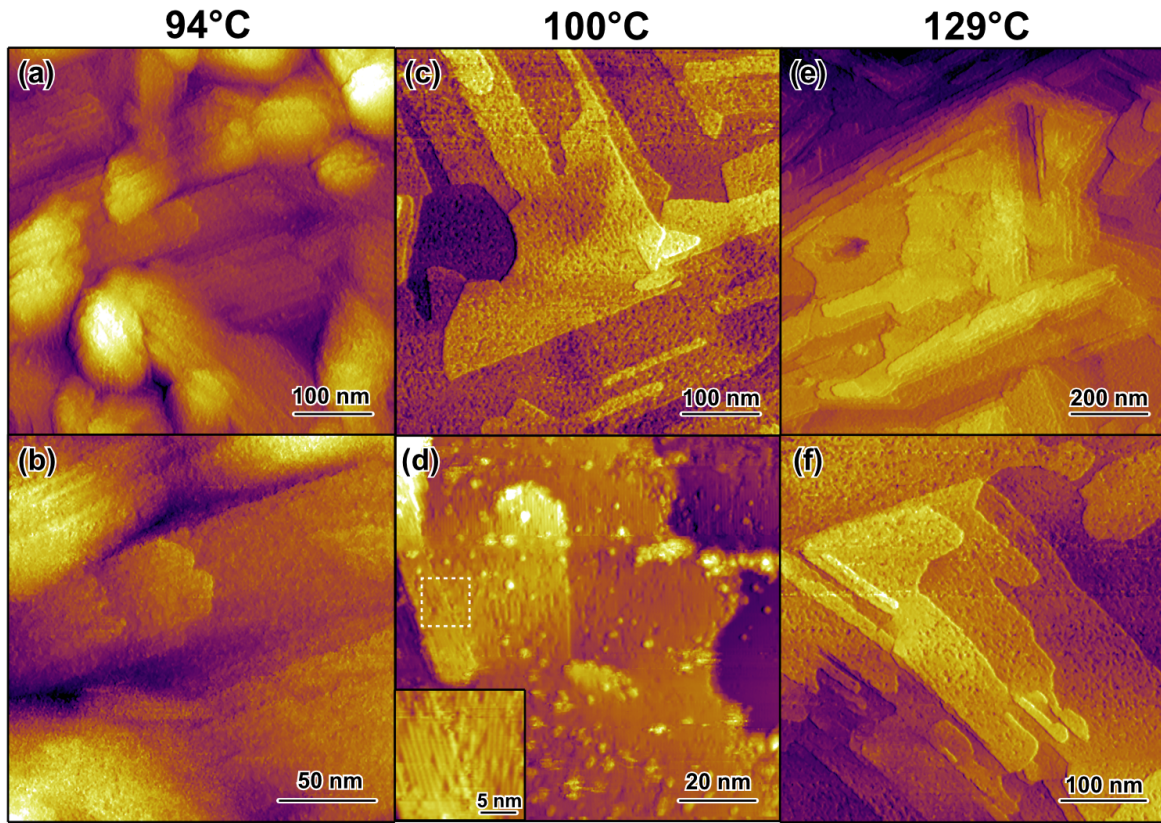


FIG. S7. Additional STM images from the three samples imaged in the main text grown at substrate temperatures of (a-b) 94 °C, (c-d) 100 °C, and (e-f) 129 °C. The RMS roughnesses (over a $500 \mu\text{m} \times 500 \mu\text{m}$ area) of areas (a) and (f) are 2.2 nm and 820 pm, respectively. In panel (d) a boundary between two rotationally misaligned domains is highlighted in the dashed region and expanded in the inset.

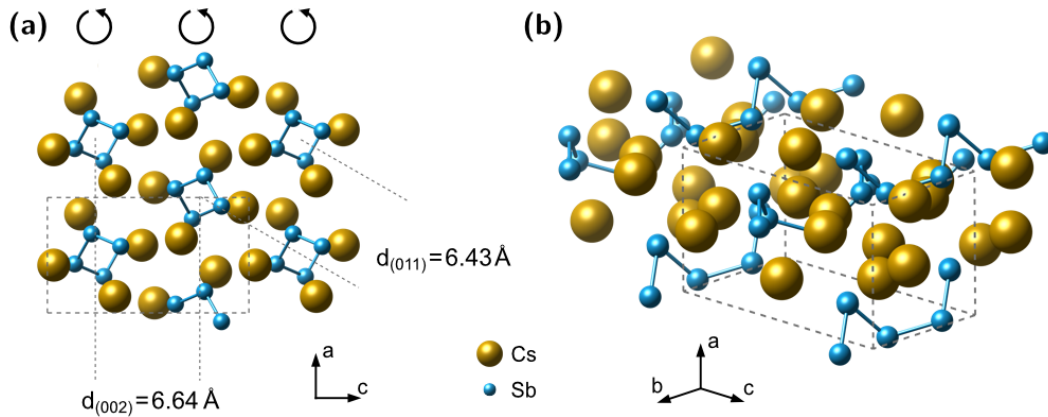


FIG. S8. Visualization of the crystal structure of the orthorhombic phase α -CsSb from crystallographic data from Ref. 11. Panel (a) is a projection down the $[010]_{or}$ axis showing the relative orientation of the Sb-Sb spirals. (b) side view of the structure showing the constant chirality of the spirals.

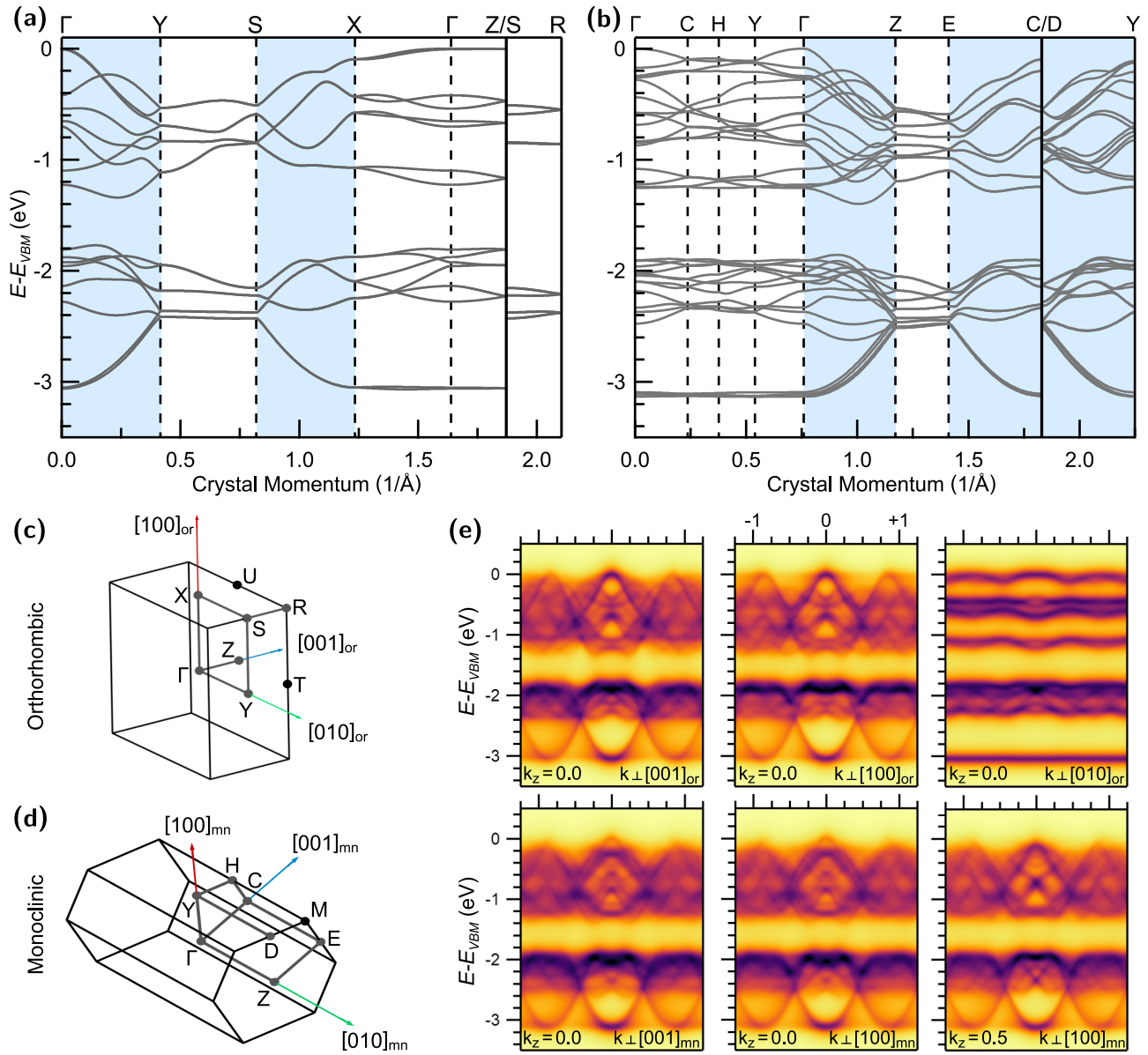


FIG. S9. Additional DFT calculations of for the α and β phases of CsSb. (a) Dispersion of α -CsSb along the path outlined in (c). (b) Dispersion of β -CsSb phase reproduced from the main text along the path of the Brillouin zone depicted in (d). In both panels, paths in a plane containing the Sb-Sb spirals are highlighted in blue. (e) Simulated spectral functions for the α (top row) and β (bottom row) phases with different choices for the film normal vector and out-of-plane momentum.

ADDITIONAL DFT CALCULATIONS

Here we present the electronic structure calculations for the orthorhombic α -CsSb structure depicted in Figure S8. The band structure of the valence bands is shown in Figure S9(a) along the path though the zone indicated in Figure S9(c). For comparison the band structure plot from the main text is reproduced in Figure S9(b). For the orthorhombic (α -CsSb) structure a plane-wave cutoff of 40 Hartrees was employed along with optimized lattice constants of $a = 7.79$ Å, $b = 7.55$ Å, and $c = 13.49$ Å obtained from a relaxation calculation. The calculations of total ground state energy and DOS employ a Brillouin zone sampling mesh of $4 \times 4 \times 4$. For efficient calculation of the electronic band structure at arbitrary crystal momenta the Wannier interpolation technique [12] is again employed. A maximally localized Wannier basis set [13] was generated using a supercell of $4 \times 4 \times 4$ orthorhombic ($4 \times 7 \times 4$ monoclinic) primitive cells and using linear combinations of bulk Bloch bands at binding energies of 0 to 11 eV below

the valence band maximum. Here and in the main text we compare the measured ARPES spectra with a simulation derived from the Wannier interpolated band structure. Because the ARPES spectrum is a sum over domains of the spectrum from each domain we can simply fix an out of plane momentum (k_z) and calculate the incoherent sum of the spectral function over azimuthally rotated cuts spaced by 0.15° . To avoid divergences a finite imaginary self energy of $\Sigma'' = 75$ meV is used as a numerical softening parameter. However, the energy width of the bands in the simulation is found to be insensitive to the specific choice of Σ'' in this limit as the main source of broadening in the calculation comes from the angular sum. Simulations of the expected spectra from both the orthorhombic α , denoted by *or*, and monoclinic β phase, denoted by *mn*, are included here as [Figure S9\(e\)](#). We do not observe a substantial difference in the simulated spectra at $k_z = 0$ between the α and β phases, other than a slightly clearer dispersion in the α phase on the top row, as a result of the very similar structure of the Sb-Sb chains. Additionally there is not a strong dependence on the out of plane momentum (bottom right). However, the alignment of the spirals perpendicular to the film normal (top right) can be confidently ruled out as it would result in a nearly flat band structure (as all dispersion would be out-of-the-plane) which is not observed in the ARPES measurements.

WORK FUNCTION ESTIMATES

Here we present the method used to estimate the workfunctions of CsSb and Cs₃Sb by extending the Dowell-Schmerge model to semiconductors. For metals, $E_F + \phi$ is the kinetic energy of the photoemitted electrons at the vacuum level where E_F is the Fermi energy and ϕ is the workfunction of the material, which can be substituted for $\phi - E_g = E_a$ for semiconductors where ϕ is the workfunction, E_g is the band gap energy, and E_a is the electron affinity. After making this substitution in Eq.7 in Dowell [14] and setting $E_F = 0$, we calculate the QE of CsSb using the DFT-calculated density of states and fitting this model with both the electron affinity and leading coefficient as free variables. We make the approximation that the reflectivity, R, of CsSb does not vary substantially across the visible range and can be treated as a constant for fitting. The equation for fitting has the form:

$$QE = A \frac{\int_{E_a-hv}^{\infty} dE f(E) D(E) D(E+ hv) \int_{\cos \theta_E}^1 d(\cos \theta)}{\int_{-hv}^{\infty} dE f(E) D(E) D(E+ hv) \int_{-1}^1 d(\cos \theta)} \quad (1)$$

Where $\cos \theta_E = \sqrt{(\phi - E_g)/(E + hv)}$. The free parameters E_a and A are then fitted to our spectral response data by minimizing a metric of the form $[\sum (\log(a_i) - \log(b_i))^2]^{\frac{1}{2}}$ where a_i are the experiment data points and b_i are the data points of the calculated spectral response. Minimizing this metric gives the electron affinity for our samples, and after adding the estimated band gap energy (0.52 eV for CsSb and 0.557 eV for Cs₃Sb) we estimate workfunctions of 1.63 eV and 2.18 eV for Cs₃Sb and CsSb respectively using this method. We also assume the dispersion in the conduction band is parabolic for CsSb, which is supported by our DFT calculations as the lower edge in the conduction band appears to be s-band.

-
- [1] R. P. Vinci, *Thin Films: Texture Effects on Mechanical Properties*, Encyclopedia of Materials: Science and Technology (Elsevier, 2001).
- [2] G. Ebbinghaus and A. Simon, Electronics structures of Rb, Cs and some of their metallic oxides studied by photoelectron spectroscopy, *Chemical Physics* **43**, 117 (1979).
- [3] M. A. H. Schmeißer, S. Mistry, H. Kirschner, S. Schubert, A. Jankowiak, T. Kamps, and J. Kühn, Towards the operation of Cs-K-Sb photocathodes in superconducting RF photoinjectors, *Phys. Rev. Accel. Beams* **21**, 113401 (2018).
- [4] L. Soriano and L. Galán, Interaction of Cesium-Potassium Antimonide Photocathode Materials with Oxygen: an X-Ray Photoelectron Spectroscopy Study, *Japanese Journal of Applied Physics* **32**, 4737 (1993).
- [5] A. Galdi, W. J. I. DeBenedetti, J. Balajka, L. Cultrera, I. V. Bazarov, J. M. Maxson, and M. A. Hines, The effects of oxygen-induced phase segregation on the interfacial electronic structure and quantum efficiency of Cs₃Sb photocathodes, *The Journal of Chemical Physics* **153**, 144705 (2020).
- [6] C. W. Bates, T. M. van Atekum, G. K. Wertheim, D. N. E. Buchanan, and K. E. Clements, X-ray photoemission studies of superficially oxidized cesium antimonide photoemitters, *Applied Physics Letters* **38**, 387 (1981).
- [7] D. J. Morgan, Metallic antimony (Sb) by XPS, *Surface Science Spectra* **24**, 024004 (2017).
- [8] A. Naumkin, A. Kraut-Vass, S. Gaarenstroom, and C. Powell, *NIST X-ray Photoelectron Spectroscopy Database* (2012).
- [9] M O Krause and J G Ferreira, K X-ray emission spectra of Mg and Al, *Journal of Physics B: Atomic and Molecular Physics* **8**, 2007 (1975).
- [10] J. Yeh and I. Lindau, Atomic subshell photoionization cross sections and asymmetry parameters: $1 \leq Z \leq 103$, *Atomic Data and Nuclear Data Tables* **32**, 1 (1985).

- [11] H. Georg von Schnering, W. Hönle, and G. Rrogull, Die Monoantimonide RbSb und CsSb, [Zeitschrift für Naturforschung B](#) **34**, 1678 (1979).
- [12] N. Marzari, A. A. Mostofi, J. R. Yates, I. Souza, and D. Vanderbilt, Maximally localized Wannier functions: Theory and applications, [Reviews of Modern Physics](#) **84**, 1419 (2012).
- [13] N. Marzari and D. Vanderbilt, Maximally localized generalized Wannier functions for composite energy bands, [Physical Review B](#) **56**, 12847 (1997).
- [14] D. H. Dowell and J. F. Schmerge, Quantum efficiency and thermal emittance of metal photocathodes, [Physical Review Special Topics - Accelerators and Beams](#) **12**, 074201 (2009).